Renewable Energy 257 (2026) 124795

Contents lists available at ScienceDirect

Renewable Energy

journal homepage: www.elsevier.com/locate/renene

Thermo-economic evaluation and working fluid screening for supercritical ORCs driven by medium-temperature geothermal sources

Qiang Liu [a,*], Fufang Yang [b], Xiong Liu [c], Xiaodong Zhang [c], Zuowei Yang [c]

[a] State Key Laboratory of Deep Geothermal Resources, College of Mechanical and Transportation Engineering, China University of Petroleum, Beijing, 102249, PR China
[b] Laboratoire de Chimie, ENS Lyon and CNRS, 46 allée d'Italie, 69364, Lyon, France
[c] Industrial Turbine Division, Dongfang Turbine Co., Ltd., Deyang, 618000, PR China

ARTICLE INFO

Keywords:
Supercritical organic Rankine cycle
Working fluid
Parameter optimization
Recuperative cycle
Geothermal power generation

ABSTRACT

This study evaluates the thermodynamic and economic performance of supercritical organic Rankine cycle (SORC) and recuperative SORC (RSORC) systems using various working fluids for medium-temperature geothermal sources (150–180 °C) with a reinjection temperature of 70 °C. Turbine inlet temperature and pressure are optimized to maximize net power output. In SORC, wet and isentropic fluids outperform dry fluids due to lower cold source losses. R134a achieves the highest net power and lowest specific investment cost (SIC) at brine temperatures below 170 °C, while R152a performs better at higher temperatures owing to reduced parasitic load. Incorporating a recuperator in RSORC improves thermal matching and, coupled with increased specific heat near the pseudocritical point, shifts the pinch point toward the low-temperature end in the primary heat exchanger, thereby reducing optimal turbine inlet temperature and pressure. Compared to SORC, RSORC narrows thermal efficiency differences among fluids, lowers parasitic power fraction (especially at lower source temperatures), but slightly increases SIC. Dry fluids generate 5.8–17.8 % more net power in RSORC than in SORC. R1234ze(E) achieves comparable net power to R134a and up to 9 % lower SIC than dry fluids, making it a promising alternative for both SORC and RSORC with lower operating pressure and reduced environmental impact.

1. Introduction

Geothermal energy has distinctive advantages such as stable temperature, high capacity factor, large storage capacity and wide distribution. The global installed geothermal power capacity reached 16.3 GW at the end of 2023, but only accounted for 0.16 % of the worldwide installed power capacity [1]. Despite the huge development potential, geothermal power generation continues to lag behind solar and wind power. While the expansion of accessible geothermal resources remains fundamental, improving thermodynamic efficiency of geothermal power cycles is also a critical factor in increasing the overall effectiveness and attractiveness of geothermal energy exploitation [2].

The organic Rankine cycle (ORC) has been widely used in commercial geothermal binary power plants [3,4], accounting for 43 % of global installations and 21.7 % of installed capacity worldwide [1]. However, simple ORCs typically achieve thermal efficiencies below 12 % for low-enthalpy geothermal resources [5,6], mainly due to temperature mismatching between the brine and the working fluid during isothermal phase change process, leading to large exergy losses. To address this, various cycle modifications have been proposed to improve thermodynamic performance [7,8]. Multi–pressure ORCs [9], such as dual- and triple-pressure configurations, offer better temperature matching with the geothermal brine, thereby decreasing irreversibility [10,11]. Parallel dual-pressure ORCs (PDORC) utilize independent evaporation circuits to achieve flexible operation [10], while series dual-pressure ORCs (SDORCs) benefit from optimized heat exchanger arrangements and flow routing to further reduce exergy losses [12,13]. Comparisons show that SDORCs often outperform PDORCs in power output [7,14]. The use of zeotropic mixtures presents another approach to improving temperature matching, thanks to their non-isothermal evaporation and condensation behaviors [15,16]. These mixtures have been evaluated in geothermal ORCs to improve net power output [17,18]. Notably, the temperature glide during condensation is typically larger than during evaporation; however, the temperature drop of brine is larger than the

* Corresponding author. State Key Laboratory of Deep Geothermal Resources, College of Mechanical and Transportation Engineering, China University of Petroleum, Beijing, 102249, PR China.

E-mail addresses: qliu@cup.edu.cn, qliuenergy@gmail.com (Q. Liu).

https://doi.org/10.1016/j.renene.2025.124795
Received 27 March 2025; Received in revised form 8 September 2025; Accepted 16 November 2025
Available online 17 November 2025

coolant temperature increase [19]. To overcome this drawback, dual-pressure systems using zeotropic mixtures [20,21] further reduce the irreversibilities during evaporation. In addition, advanced ORC designs have incorporated composition tuning of zeotropic mixtures to adapt to varying heat source conditions [22,23], which increased in net power output and reduced electricity production cost compared to conventional ORCs [24]. However, further power gains were limited under optimal control strategies [25].

Beyond evaporation-based cycles, the trilateral cycle (TLC) eliminates isothermal phase change and enables near-perfect temperature matching with the heat source [26,27]. DiPippo [28] noted that TLCs set a more realistic upper bound for thermal efficiency. Fischer [29] reported 14−29 % higher exergy efficiency of a TLC than a traditional ORC. Nevertheless, TLCs are challenged by high volumetric flow rate at the expander outlet, and their application remains constrained by the performance of two-phase expanders, which rarely exceed 75 % isentropic efficiency [28]. Partial-evaporating ORCs provide another means of improving temperature matching [30,31]. The theoretical and experimental studies demonstrated that partial evaporating ORCs presented higher efficiency than traditional cycles [32,33]. When zeotropic mixtures are used in partial evaporation ORCs, further performance gains are observed [34,35], yet, as with TLCs, the development of efficient and robust two-phase expanders remains a major technical bottleneck [36]. To bypass two-phase expansion, organic flash cycles (OFCs) [37] have been introduced. These systems present the favorable heat addition profile of TLCs by using throttling valves and flash separators [38]. Regenerative OFCs [39], double flash OFCs [40], and regenerative double flash cycles [41] were developed to recover the sensible heat of the saturated liquid stream. However, the throttling valves created large irreversibility losses in an OFC. Replacing the throttling valves with two-phase expanders has been shown to improve net power output by up to 16.6 % [42]. Combining the concepts of OFC and partial evaporation, the organic Rankine flash cycle (ORFC) integrates a flash evaporator and achieves higher thermal efficiency along with better economic performance [43,44].

In a supercritical ORC (SORC), the working fluid is pressurized beyond its critical point, thereby eliminating the isothermal phase change characteristic of subcritical cycles. This enables a more favorable temperature profile alignment between the geothermal brine and the working fluid, reducing exergy losses during heat absorption. On the *T-s* diagram, SORCs resemble triangular shape with continuous heating [30,45], but unlike TLCs, the expansion process occurs entirely in the vapor region, resulting in higher isentropic efficiency and lower volumetric expansion ratio [5]. Additionally, SORCs can extract more heat from the geothermal brine, enhancing exergy utilization and lowering brine consumption per unit of net power [46,47]. SORCs present superior thermal efficiencies compared to subcritical cycles [48,49], owing to a higher mean effective temperature during heat addition and reduced irreversibilities. Moreover, SORCs present a simpler alternative to multi-pressure evaporative ORCs while maintaining a desirable heating curve profile [4]. Field applications further validate these advantages: SORCs deployed at the San Emidio and Neal Hot Springs plants outperform the dual-pressure ORC using R601a at the Raft River site in terms of net exergy utilization efficiency [47]. Given the growing interest in ORCs for medium-temperature geothermal applications [1], there is increasing motivation to explore the thermodynamic and economic characteristics of SORCs. This includes selecting environmentally friendly working fluids with favorable thermal stability and safety, and evaluating the techno-economic trade-offs to support their broader deployment.

Working fluid selection plays a crucial role in the performance of SORC systems utilizing medium-to-low grade heat sources [46,50]. Early studies mainly focused on pure working fluids such as hydrocarbons and hydrofluorocarbons (HFCs). Schuster et al. [45] demonstrated that SORC using R365mfc achieved an increase of 8 % in thermal efficiency over subcritical cycles at a source temperature of 210 °C. Augustine et al. [46] identified R134a as the most suitable working fluid for SORCs operating between 140 and 170 °C, delivering 6.4−22.5 % more net power output than subcritical cycles. Similar conclusions were reached by Invernizzi and Bombarda [51] for the 140–200 °C range, and by Toffolo et al. [49], who observed 1.9–16.8 % higher net power output for SORCs with R134a over subcritical ORCs with R600a for the 130−170 °C geothermal sources. Gu and Sato [48] compared thermodynamic performance of R134a, R125, and R290 for a 229 °C heat source, recommending R134a and R290. Expanding the range of fluids and performance metrics, Vidhi et al. [52] assessed various HFCs and hydrocarbons in regenerative SORCs (RSORCs), identifying R134a as superior in thermal and exergy efficiencies for geothermal sources between 130 and 200 °C. A broader parametric study by Moloney et al. [53] identified R1233zd(E), R600, R601a and R601 as optimal fluids for RSORCs in the 181−251 °C range. Lukawski et al. [54] studied how fluid molecular structure affected cycle efficiencies of SORC and RSORC for source temperatures between 100 °C and 230 °C. Yang et al. [55] used a corresponding state model to map the thermal efficiency and volumetric power output limits of SORCs. Wang et al. [56] identified R134a, R32, R600a and R22 as promising fluids for SORC driven by hot CO_2 at 195 °C. Zhang et al. [57] recommended R142b as the working fluid for SORC driven by two-phase geothermal fluids. While HFCs have shown favorable thermodynamic characteristics [58], their high global warming potentials (GWPs) pose regulatory challenges under the Kigali Amendment. As an alternative, zeotropic mixtures introduce temperature glide during phase change, enabling non-isothermal condensation and improved thermal matching [59,60]. Their potential benefits in SORC applications have been demonstrated [61,62]. However, their application is limited by significantly increased heat exchanger areas and associated capital costs [5,63].

The turbine inlet parameters strongly affect the thermodynamic performance of SORCs. Schuster et al. [45] analyzed the impact of turbine inlet temperature on thermal and exergy efficiencies. Vidhi et al. [52] studied how pressure ratio and turbine inlet pressure affect thermal efficiency to determine optimal operating conditions. Moloney et al. [53] optimized turbine inlet pressure for maximum plant efficiency under given inlet temperature, disregarding brine reinjection temperature constraints. Toffolo et al. [49] conducted a multi-variable optimization using the Heatsep method to maximize the exergy recovery efficiency (net power output) for SORC with R134a. Similarly, Manente et al. [64] optimized the turbine inlet parameters for six working fluids, considering the effect of expansion ratio on turbine isentropic efficiency. Maraver et al. [65] conducted a parametric optimization to identify the highest exergy efficiencies for SORCs utilizing geothermal heat at 170 °C. Le et al. [66] optimized the turbine inlet parameters, condensation temperature and brine outlet temperature to maximize the efficiencies of SORCs and RSORCs using genetic algorithm, highlighting how optimal parameters and working fluid selection are sensitive to the chosen optimization criteria. Astolfi et al. [67] performed a multivariable optimization on turbine inlet pressure and approach point temperature difference to compare six ORC configurations. They found that SORC was optimal when there were no constraints on brine reinjection temperature, whereas RSORCs performed better when such constraints were present. In a follow-up techno-economic analysis [68], they incorporated turbine design and isentropic efficiency prediction into a multi-criteria framework to minimize specific investment cost. To explore trade-offs between thermodynamic and economic performance, Song et al. [69] carried out a multi-objective optimization using the NSGA-II algorithm to maximize exergy efficiency and minimize the payback period. Their results identified that non-recuperated SORCs were preferable for medium-temperature geothermal sources, especially when the working fluids with critical temperature aligned closely with the source temperature. Wang et al. [70] applied the TLFD-GA algorithm for multi-objective optimization targeting thermodynamic, environmental, and economic metrics. They concluded that SORC outperformed RSORC when accounting for pressure losses. From a sustainability perspective, Heberle et al. [71] conducted a life-cycle assessment of subcritical and supercritical ORCs using representative German geothermal resources. For low-temperature sources with unrestricted reinjection temperature, SORC achieved 37 % higher exergy efficiency and lower CO_2-equivalent emissions. However, for high-temperature sources with reinjection temperature limits, the thermodynamic and environmental advantages of SORCs diminished.

Despite extensive investigations into working fluid selection, parametric optimization and multi-objective assessments of SORC systems, several challenges remain. Traditional fluids such as hydrofluorocarbons (HFCs) and hydrocarbons either present high global warming potentials (GWPs) or face safety concerns like flammability, prompting a shift toward low-GWP alternatives such as R1234yf, R1234ze(E), and R1243zf. Although these next-generation fluids have shown promising environmental characteristics, comprehensive thermodynamic comparisons under realistic geothermal constraints are still limited. Moreover, the effectiveness of RSORC configurations strongly depends on working fluid properties, cycle parameters, and heat-source conditions. The influence of fluid thermophysical properties and cycle parameters on recuperator feasibility remains insufficiently characterized, especially under medium-temperature geothermal applications.

This study aims to optimize the turbine inlet temperature and pressure for representative working fluids to maximize the net power output of both SORC and RSORC configurations applied to medium-temperature geothermal sources (150–180 °C), with a reinjection temperature of 70 °C. The thermodynamic impacts of turbine inlet parameters are comprehensively analyzed, emphasizing the differing responses of SORC and RSORC due to the presence of a recuperator. In particular, the coupled effects of turbine inlet parameters and working fluid thermophysical properties on the location of the pinch point in the primary heat exchanger are investigated. Furthermore, the thermodynamic and economic characteristics are evaluated for both environmentally friendly alternatives (R1234yf, R1234ze(E), R1243zf) and conventional fluids (R134a, R290, RC318, R152a, R227ea).

2. Methodology

2.1. System description

Fig. 1 shows the schematic configurations of a SORC and a recuperative SORC (RSORC). Fig. 2 shows the corresponding temperature-entropy diagrams. The working fluid is heated to supercritical state by the geothermal brine in the primary heat exchanger (PHE). The supercritical fluid goes through the turbine and expands to produce power. The turbine exhaust vapor is cooled to subcooled liquid in the condenser by the cooling water. The subcooled liquid is compressed by the working fluid pump to a supercritical pressure and then goes through the PHE again to repeat the cycle. A recuperator is used to recover the waste heat from the superheated vapor exhausted from the turbine to preheat the working fluid from the pump in a RSORC. The PHE inlet temperature can be improved to increase the cycle efficiency and reduce the irreversibility losses.

2.2. Working fluid selection

Working fluid has significant impact on the thermodynamic and

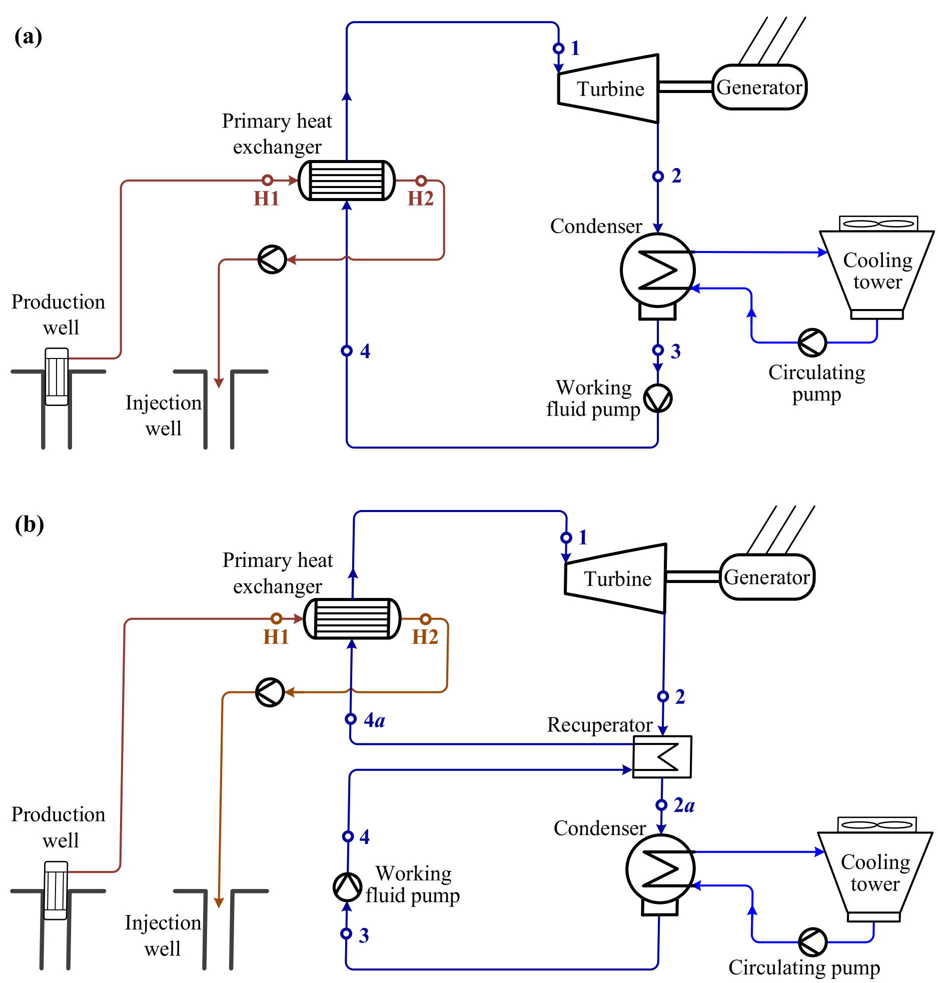

Fig. 1. Schematic diagrams for (a) a SORC and (b) a recuperative SORC (RSORC).

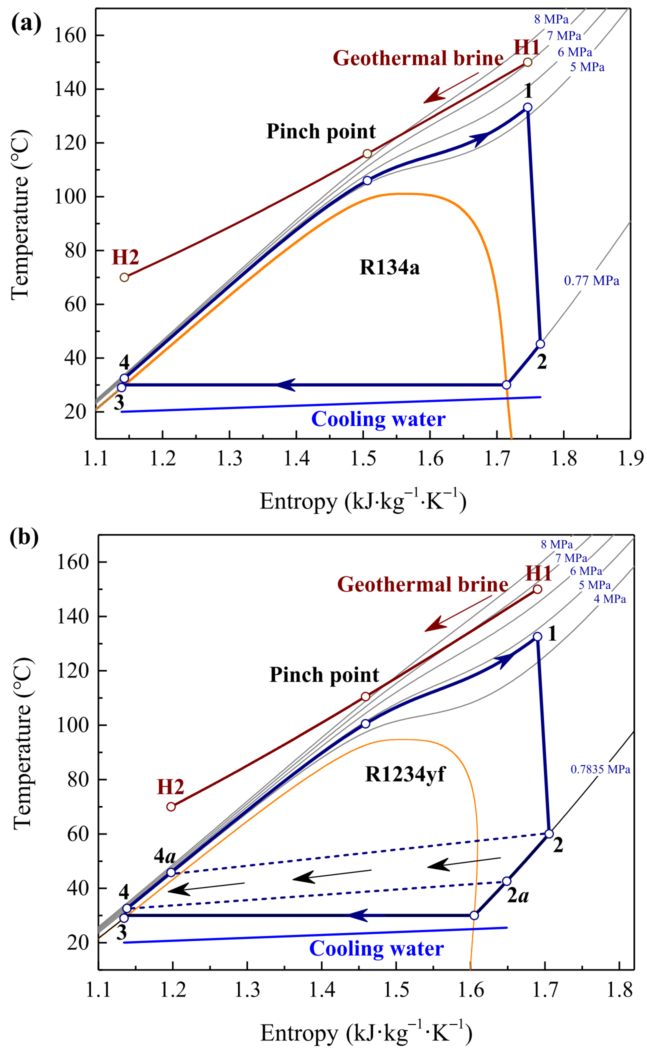

Fig. 2. Temperature-entropy diagrams for (a) SORC and (b) RSORC.

economic performance of the ORC [54,58]. The selection of thermodynamically efficient and environmentally friendly working fluid is a crucial approach for geothermal power generation system design. In this work, HFCs (hydrofluorocarbons), HCs (hydrocarbons) and HFOs (hydrofluoroolefins) were considered as the supercritical ORCs working fluids. R134a and R290 (propane) have been used in commercial binary power plants [3,47]. R227ea and R152a have also been widely studied as supercritical ORC working fluids. However, R134a and R227ea are progressively being phased out because of their higher GWPs (global warming potentials). Thus, the low GWP alternatives R1234yf (2,3,3,3-tetrafluoroprop-1-ene), R1243zf (3,3,3-Trifluoropropene) and R1234ze(E) (trans-1,3,3,3-Tetrafluoropropene) were considered as SORC working fluids. RC318, which has a lower critical pressure, was also considered. The selected fluids ensure operational safety and present good thermal stability under supercritical pressures [72,73] and the highest cycle temperatures [74,75].

Table 1 lists the properties and Fig. 3 shows the temperature-entropy diagrams of the saturation curves of the candidate working fluids. The working fluids can be categorized as wet, dry and isentropic types according to the saturation vapor curve. R290, R134a and R152a have a negative saturation vapor curve ($dT/ds < 0$) in a temperature–entropy diagram, but only R152a expands into the two–phase region for brine temperatures below 172 °C. An isentropic fluid has a nearly vertical vapor saturation curve. Here, R1243zf and R1234ze(E) can be regarded as isentropic fluids.

Table 1
Properties of the working fluid candidates.

Working fluid	Critical temperature (°C)	Critical pressure (MPa)	GWP	Safety Classification	Fluid type
R1234yf	94.7	3.3822	1	A2L	dry
R290	96.74	4.2512	3.3	A3	wet
R134a	101.06	4.0593	1430	A1	wet
R227ea	101.75	2.925	3220	A1	dry
R1243zf	103.78	3.5179	1	A1	isentropic
R1234ze(E)	109.363	3.6349	6	A2L	isentropic
R152a	113.261	4.5168	124	A2	wet
RC318	115.23	2.7775	10300	A1	dry

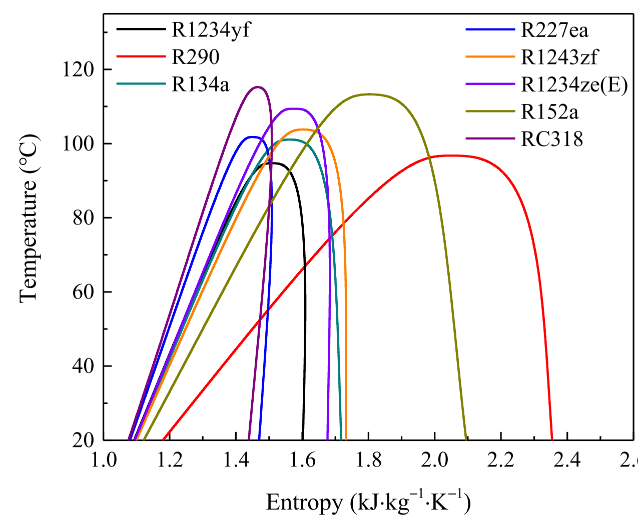

Fig. 3. *T-s* diagrams of the saturation curves of the working fluid candidates.

2.3. Thermodynamic model

The heat input to the working fluid from the geothermal brine in the primary heat exchanger (PHE) is

$$\dot{Q}_{in} = \dot{m}_G(h_{H1} - h_{H2}) = \dot{m}_O(h_1 - h_4) \tag{1}$$

where $\dot{m}_G$ is the geothermal brine mass flow rate, h_{H1} and h_{H2} are the brine specific enthalpies at the PHE inlet and outlet, $\dot{m}_O$ is the working fluid mass flow rate, and h_1 and h_4 are the working fluid specific enthalpies at the PHE outlet and inlet.

The power generated by the turbine is

$$\dot{W}_T = \dot{m}_O(h_1 - h_2) \tag{2}$$

where h_2 is the actual specific enthalpy at the turbine exhaust.

The energy balance for the recuperator can be simplified as

$$h_2 - h_{2a} = h_{4a} - h_4 \tag{3}$$

where h_{2a} is the specific enthalpy of the vapor at the recuperator outlet and h_{4a} is the specific enthalpy of the pressurized liquid leaving the recuperator.

The power consumed by the working fluid feed pump is calculated as

$$\dot{W}_{FP} = \dot{m}_O(h_4 - h_3) \tag{4}$$

The cycle thermal efficiency is given by

$$\eta_{cyc} = \frac{\dot{W}_T - \dot{W}_{FP}}{\dot{Q}_{in}} = 1 - \frac{\dot{Q}_2}{\dot{Q}_{in}} \tag{5}$$

where $\dot{Q}_2$ is the heat losses to the cold source.

The cooling water mass flow rate is determined by

$$\dot{m}_{\mathrm{CW}} = \frac{\dot{Q}_2}{c_{p,\mathrm{W}} \Delta t_{\mathrm{CW}}} \tag{6}$$

where $c_{p,\mathrm{W}}$ is the cooling water specific heat at constant pressure and Δt_{CW} is the cooling water temperature increase.

The power consumed by the cooling water circulating pump is given by

$$\dot{W}_{\mathrm{CP}} = \frac{\dot{m}_{\mathrm{CW}} g H}{\eta_{\mathrm{CP}} \eta_{\mathrm{MO}}} \tag{7}$$

where g is the gravitational acceleration, H is the pump head, η_{CP} is the circulating pump efficiency and η_{MO} is the motor efficiency.

The power consumed by the cooling tower fan is expressed as

$$\dot{W}_{\mathrm{CTF}} = \frac{\dot{V}_{\mathrm{a}} \Delta p_{\mathrm{a}}}{\eta_{\mathrm{F}} \eta_{\mathrm{MO}}} \tag{8}$$

where $\dot{V}_{\mathrm{a}}$ is the volumetric flow rate of air, Δp_{a} is the air pressure increase, and η_{F} is the fan efficiency.

The net power output of the system is

$$\dot{W}_{\mathrm{net}} = \dot{W}_{\mathrm{T}} \eta_{\mathrm{m}} \eta_{\mathrm{g}} - \dot{W}_{\mathrm{FP}} - \dot{W}_{\mathrm{CP}} - \dot{W}_{\mathrm{CTF}} \tag{9}$$

The net thermal efficiency of the system is

$$\eta_{\mathrm{th}} = \frac{\dot{W}_{\mathrm{net}}}{\dot{Q}_{\mathrm{in}}} \tag{10}$$

The exergy input from the geothermal brine is

$$\dot{E}_{\mathrm{G,in}} = \dot{m}_{\mathrm{G}} [(h_{\mathrm{H1}} - h_0) - T_0 (s_{\mathrm{H1}} - s_0)] \tag{11}$$

where the subscript 0 represents the reference state, T_0 was assumed to be 293.15 K.

The exergy destruction rate in each component is

$$\Omega_i = \frac{\dot{I}_i}{\dot{E}_{\mathrm{G,in}}} \tag{12}$$

where $\dot{I}_i$ is the exergy destruction in the component.

The net exergy efficiency of the system is

$$\eta_{\mathrm{ex}} = \frac{\dot{W}_{\mathrm{net}}}{\dot{E}_{\mathrm{G,in}}} \tag{13}$$

2.4. Case studies and parameter optimization

Table 2 lists the operating parameters and boundary conditions for the supercritical ORCs. The geothermal brine reinjection temperature was set to 70 °C [65,67] to avoid scaling and fouling problems. The pinch point temperature difference was set to 10 °C for the PHE and recuperator [46,49] and 5 °C for the condenser [49,76]. The condensation temperature was assumed to be 30 °C. The thermodynamic properties of the working fluids and the geothermal brine were calculated using REFPROP 10.0 [77]. The turbine inlet temperature and pressure were simultaneously optimized to maximize the cycle net power output using MATLAB for brine inlet temperatures from 150 °C to 180 °C. The parameter optimization flow chart is shown in Fig. 4. The turbine inlet temperature, T_1, was constrained to be within [$1.025T_{\mathrm{cr}}$, $T_{\mathrm{Gin}}-10$] and the pressure was constrained to be above $1.05p_{\mathrm{cr}}$. The turbine exhaust quality should be higher than 90 % for a wet working fluid [46,52].

The location of the pinch point within the PHE is governed by the heat capacity rates of the geothermal brine and the working fluid, defined as the product of their mass flow rates and the specific heat. As the working fluid goes through the large specific heat region near the pseudocritical temperature, a substantial amount of heat is absorbed with only a small temperature increase. Consequently, the relative magnitudes of the heat capacity rates determine where the temperature profiles of the two streams converge to the minimum approach, as shown in Fig. 5. Crucially, both the mass flow rate and specific heat of the working fluid strongly depend on the turbine inlet parameter. As a result, the pinch point location cannot be predefined. In this work, the pinch point location in the PHE is determined using an iterative procedure [66,67], wherein the PHE is divided into 200 equal heat duty segments to calculate the local temperature difference between the brine

Table 2
Operating parameters and boundary conditions for the supercritical ORCs.

Parameters	Value
Geothermal brine mass flow rate	50 kg s $^{-1}$
Geothermal brine pressure	1 MPa
Geothermal brine reinjection temperature	70 °C
Cooling water inlet temperature	20 °C
Condensation temperature	30 °C
Pinch point temperature difference in the PHE	10 °C
Pinch point temperature difference in the recuperator	10 °C
Pinch point temperature difference in the condenser	5 °C
Subdegree of working fluid at the condenser outlet	1 °C
Turbine isentropic efficiency	85 %
Mechanical efficiency	98 %
Generator efficiency	98 %
Working fluid feed pump isentropic efficiency	75 %
Circulating pump efficiency	80 %
Circulating pump head	20 m
Cooling tower fan efficiency	65 %
Cooling tower fan pressure increase	170 Pa
Motor efficiency	95 %

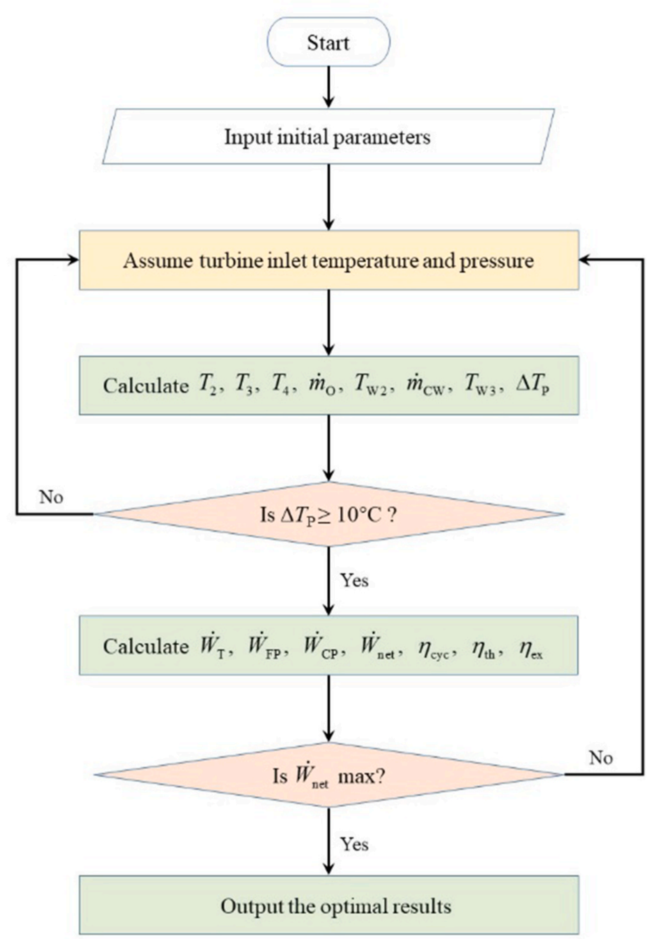

Fig. 4. Parameter optimization flow chart for supercritical ORCs.

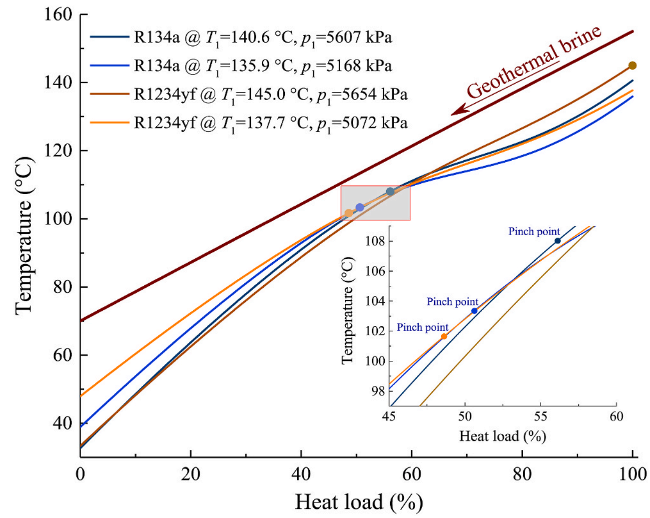

Fig. 5. *T-Q* diagram of typical working fluids in the PHE.

and the working fluid. The minimum temperature difference in each segment is constrained not to fall below 10 °C by adjusting the turbine inlet pressure and temperature iteratively, while optimizing the net power output.

The energy balance for the *i*th segment is

$$\dot{Q}_i = \dot{m}_G c_{p,G,i}\left(T_{G,i}^{in} - T_{G,i}^{out}\right) = \dot{m}_O c_{p,O,i}\left(T_{O,i}^{out} - T_{O,i}^{in}\right) \tag{14}$$

where $c_{p,G,i}$ is the average specific heat of the geothermal brine in the *i*th segment, $T_{G,i}^{in}$ and $T_{G,i}^{out}$ are the brine temperature at the *i*th segment inlet and outlet, respectively; $T_{O,i}^{in}$ and $T_{O,i}^{out}$ are the working fluid temperature at the *i*th segment inlet and outlet, respectively; and $c_{p,O,i}$ is the average specific heat of the working fluid.

2.5. Validation of the optimization framework

To validate the accuracy of the thermodynamic optimization framework, the turbine inlet temperature (T_1) and pressure (p_1), and condensation temperature (T_{con}) were optimized following the procedure outlined in Section 2.4 for a supercritical ORC with a dry cooling system using R134a as the working fluid, adopting the same boundary conditions from Ref. [49]. Table 3 lists the optimal parameters and thermodynamic indictors for geothermal brine temperature ranging from 150 °C to 180 °C. The differences in condensation temperature were within 0.2 °C. The maximum deviations observed were 2.6 °C in turbine inlet temperature and 0.45 MPa in turbine inlet pressure, which can be attributed to the method used to evaluate the temperature difference between the brine and R134a. In addition, over a relatively broad range of turbine inlet temperatures, when the inlet pressure is set by the pinch point limitation, the net power output presents only minor variation; thus, there is a narrow operational window in which turbine inlet pressure varies significantly with inlet temperature, yet the net power output remains relatively insensitive. Notably, the differences in net power output were within 1 %, confirming the thermodynamic consistency of our approach. The slight deviations between the optimized results of this study and those reported in Ref. [49] confirm the reliability and precision of our optimization approach.

2.6. Heat transfer area

All the heat exchangers are modeled as counter-flow shell-and-tube types. To capture detailed variations in thermophysical properties and temperature difference, the PHE is discretized into 200 segments, while the condenser, recuperator, and desuperheater are each divided into 40 segments. The heat transfer area of the *i*th segment is calculated as

$$A_i = \frac{\dot{Q}_i}{U_i \Delta T_{LM,i}} \tag{15}$$

The logarithmic mean temperature difference (LMTD) in *i*th segment is

$$\Delta T_{LM,i} = \frac{\Delta T_{max,i} - \Delta T_{min,i}}{\ln\left(\Delta T_{max,i} / \Delta T_{min,i}\right)} \tag{16}$$

The overall heat transfer coefficient (HTC), U_i, for *i*th segment is determined as

$$\frac{1}{U_i} = \frac{1}{\alpha_{in}}\frac{d_o}{d_{in}} + R_{in}\frac{d_o}{d_{in}} + R_o + \frac{\delta}{\lambda}\frac{d_o}{d_m} + \frac{1}{\alpha_o} \tag{17}$$

where α_{in} and α_o are the HTCs on the internal and external surfaces of the tube, respectively; R_i is the internal fouling thermal resistance, assumed to be 1.76×10^{-4} m^2 (K W)$^{-1}$, and R_o is the external fouling thermal resistance, taken as 1.76×10^{-4} m^2 (K W)$^{-1}$ for temperatures below 52 °C and 3.52×10^{-4} m^2 (K W)$^{-1}$ for temperatures above 52 °C, d_i and d_o are the inner and outer diameters of the tube, d_m is the logarithmic mean tube diameter, $d_m = \frac{d_o - d_{in}}{\ln(d_o/d_{in})}$, δ is the tube wall thickness, and λ is the thermal conductivity of the tube wall (316 stainless steel), assumed to be 17 W (m K)$^{-1}$.

In the PHE, the working fluid at supercritical pressure flows inside the tubes, while the geothermal brine circulates on the shell side. The velocity of the working fluid at PHE inlet is set to 1.5 m/s. In the condenser and desuperheater, the cooling water flows inside the tubes, whereas the working fluid is routed through the shell side. The velocity of the turbine exhaust vapor at the desuperheater or recuperator inlet is set to 15 m/s. Assuming that all heat exchangers operate as steady-state open systems, the fluid velocity in each segment is adjusted based on density variations induced by temperature changes [78].

The HTC of the working fluid at supercritical pressure flowing inside

Table 3
Validation of the parameter optimization approach with Ref. [49].

Parameter	Ref. [49]				This work			
$T_{G,in}$ (°C)	150	160	170	180	150	160	170	180
p_1 (MPa)	4.797	5.257	5.864	6.67	4.847	5.489	6.267	7.120
T_1 (°C)	129.4	139.4	149.3	159.3	128.9	140.4	151.5	161.9
p_2 (MPa)	0.8323	0.8319	0.8308	0.8286	0.8356	0.8329	0.8304	0.8276
T_{con} (°C)	32.7	32.7	32.7	32.6	32.9	32.8	32.6	32.5
$\dot{m}_O$ (kg·s^{-1})	159.5	177.4	195	212.1	160.0	177.5	194.8	211.7
$\dot{m}_{air,ACC}$ (kg·s^{-1})	3785	4225	4680	5170	3744.1	4230.0	4723.8	5239.8
$\dot{W}_T$ (kW)	4822.9	5882.9	7039.9	8316.8	4793.2	5920.2	7147.8	8463.8
$\dot{W}_{FP}$ (kW)	757	939.3	1172.8	1478.3	768.6	988.6	1264.4	1588.3
$\dot{W}_{ACC}$ (kW)	567.8	634	702.2	775.6	561.6	634.5	708.6	786.0
$\dot{W}_{net}$ (kW)	3498.1	4309.6	5165	6062.9	3463.0	4297.0	5174.8	6089.6
η_{ex} (%)	44.5	46.7	48.4	49.8	44.00	46.55	48.50	49.97
η_{th} (%)	10.33	11.29	12.15	12.93	10.23	11.26	12.17	12.98

the PHE and recuperator tubes is calculated using the correlation developed by Morky et al. [79], given by

$$\alpha_{in} = 0.0061 \frac{\lambda_b}{d_{in}} Re_b^{0.904} \overline{Pr}_b^{0.684} \left(\frac{\rho_w}{\rho_b}\right)^{0.564} \tag{18}$$

where $\overline{Pr}_b = \frac{\mu_b \bar{c}_p}{\lambda_b}$, $\bar{c}_p = \frac{h_w - h_b}{T_w - T_b}$, T_b and T_w are the bulk fluid temperature and the inner wall temperature, respectively; h_b and h_w are the specific enthalpies at the bulk fluid and inner wall temperatures, respectively; ρ_b and ρ_w are the densities at the bulk fluid and inner wall temperatures, and λ_b is the thermal conductivity at the bulk fluid temperature.

The condensation HTC of the working fluid on the external surface of plain horizontal tubes in the condenser is calculated using the correlation [80].

$$\alpha = 0.79 \left[\frac{r \lambda_{SL}^3 \rho_{SL} (\rho_{SL} - \rho_{SV}) g}{\mu_{SL} d_o (T_s - T_w)}\right]^{0.25} \tag{19}$$

where r is the working fluid latent heat, μ_{SL} is the saturated liquid dynamic viscosity, ρ_{SL} and ρ_{SV} are the saturated liquid and vapor densities, T_s is the saturation temperature and T_w is the tube wall temperature.

The HTC of the cooling water flowing inside the condenser and desuperheater tubes is determined using the Gnielinski correlation [81].

$$\alpha_{in} = \frac{\lambda}{d_{in}} \frac{(f/8)(Re - 1000)Pr}{1 + 12.7 (f/8)^{1/2} (Pr^{2/3} - 1)} \tag{20}$$

where $f = [0.79 \ln(Re) - 1.64]^{-2}$.

The shell-side HTC for the working fluid in the recuperator and desuperheater, as well as for the geothermal brine in PHE, is calculated using the Churchill-Bernstein correlation [82].

$$\alpha_o = \frac{\lambda}{d_o} \left[0.3 + \frac{0.62 Re^{1/2} Pr^{1/3} \left(1 + (Re/282000)^{5/8}\right)^{4/5}}{\left(1 + (0.4/Pr)^{2/3}\right)^{1/4}}\right] \tag{21}$$

2.7. Economic model

The module costing technique has been widely adopted for evaluating the cost of ORC systems [49,69]. In this study, the cost correlations developed by Turton et al. [83] are employed to assess the economic performance of both the SORC and RSORC using various working fluids. The purchased cost under base conditions (equipment constructed from carbon steel and operating at near-ambient pressures) is calculated as

$$\log_{10}(C_P^0) = K_1 + K_2 \log_{10}(X) + K_3 [\log_{10}(X)]^2 \tag{22}$$

where X is the equipment capacity or size parameter (power output or heat exchanger area), and K_1, K_2 and K_3 are component-specific constants listed in Table 4.

The pressure factor, F_p, which accounts for variations in operating pressure, is given as

$$log_{10}(F_p) = C_1 + C_2 \, log_{10}(p) + C_3 [log_{10}(p)]^2 \tag{23}$$

where p is the gauge pressure and C_1, C_2 and C_3 are component and type specific coefficients provided in Table 4.

Thus, the bare module equipment cost [83] is

$$C_{BM} = C_P^0 F_{BM} = C_P^0 (B_1 + B_2 F_p F_M) \tag{24}$$

where F_{BM} is the bare module cost factor, B_1 and B_2 are constants, and F_M is the material factor, as specified in Table 4.

The generator capacity is oversized by 10 % relative to the turbine power output. The cost of the generator is estimated using the correlation provided in [49].

$$C_{P,GEN}^0 = 1.85 \times 10^6 \left(\frac{\dot{W}_{GEN}}{11800}\right)^{0.94} \tag{25}$$

The cost of cooling tower is estimated using the correlation [84].

$$C_{P,CT}^0 = C_1 \dot{m}_{CW}^{C_2} 10^{C_3 \Delta t_{ap} \Delta t_{CW} + K_1 \Delta t_{ap} + K_2 \Delta t_{CW} + K_3} \tag{26}$$

where C_1, C_2, C_3, K_1, K_2, and K_3 are the coefficients listed in Table 4, and Δt_{ap} is the difference between the cooling water temperature at the cooling tower outlet and the ambient air wet-bulb temperature.

The specific investment cost of the supercritical ORC systems is defined as

$$SIC = \frac{\sum C_{BM}}{\dot{W}_{net}} \tag{27}$$

3. Parametric analysis

The effects of turbine inlet temperature and pressure on the thermodynamic performance of SORC and RSORC are analyzed in this section. Then, the optimized turbine inlet parameters corresponding to the maximum net power output for selected working fluids are presented and compared.

3.1. Effect of turbine inlet parameters on power output in SORC

Fig. 6 shows the influences of turbine inlet temperature and pressure on the turbine power outputs of SORCs using typical working fluids. When the turbine inlet pressure is relatively low, increasing the turbine inlet temperature results in only a slight increase in turbine power output, because the increase in specific enthalpy drop is offset by the decrease in working fluid mass flow rate. In contrast, at higher turbine inlet pressures, increasing the inlet temperature leads to a more significant increase in the specific enthalpy drop (see Fig. 7), resulting in a noticeable increase in turbine power output. For a given turbine inlet temperature, the working fluid mass flow rate increases as the inlet pressure increases because the average specific heat decreases while the PHE inlet temperature slightly increases. Meanwhile, the decrease in turbine exhaust temperature leads to a higher cycle efficiency.

Table 4
Coefficients used for the estimation of capital costs for each component [83,84].

Coefficients	Heat exchanger	Turbine	Pump	Generator	Motor	Cooling tower	Fan
X	A (m^2)	$\dot{W}$ (kW)	$\dot{W}$ (kW)	$\dot{W}$ (kW)	$\dot{W}$ (kW)	$\dot{m}$ (kg/s)	$\dot{V}$ (m^3/s)
K_1	4.3247	2.7051	3.3892	/	2.4604	−0.026719	3.1761
K_2	−0.3030	1.4398	0.0536	/	1.4191	0.043654	−0.1373
K_3	0.1634	−0.1776	0.1538	/	−0.1798	−0.1026	0.3414
C_1	0.03881	/	−0.3935	/	/	3950.9	/
C_2	−0.11272	/	0.3957	/	/	0.58729	/
C_3	0.08183	/	−0.00226	/	/	−0.0032091	/
B_1	1.63	/	1.89	/	/	/	/
B_2	1.66	/	1.35	/	/	/	/
F_M	1.8	/	1.5	/	/	/	/
F_{BM}	/	3.5	/	1.5	1.5	4	2.8

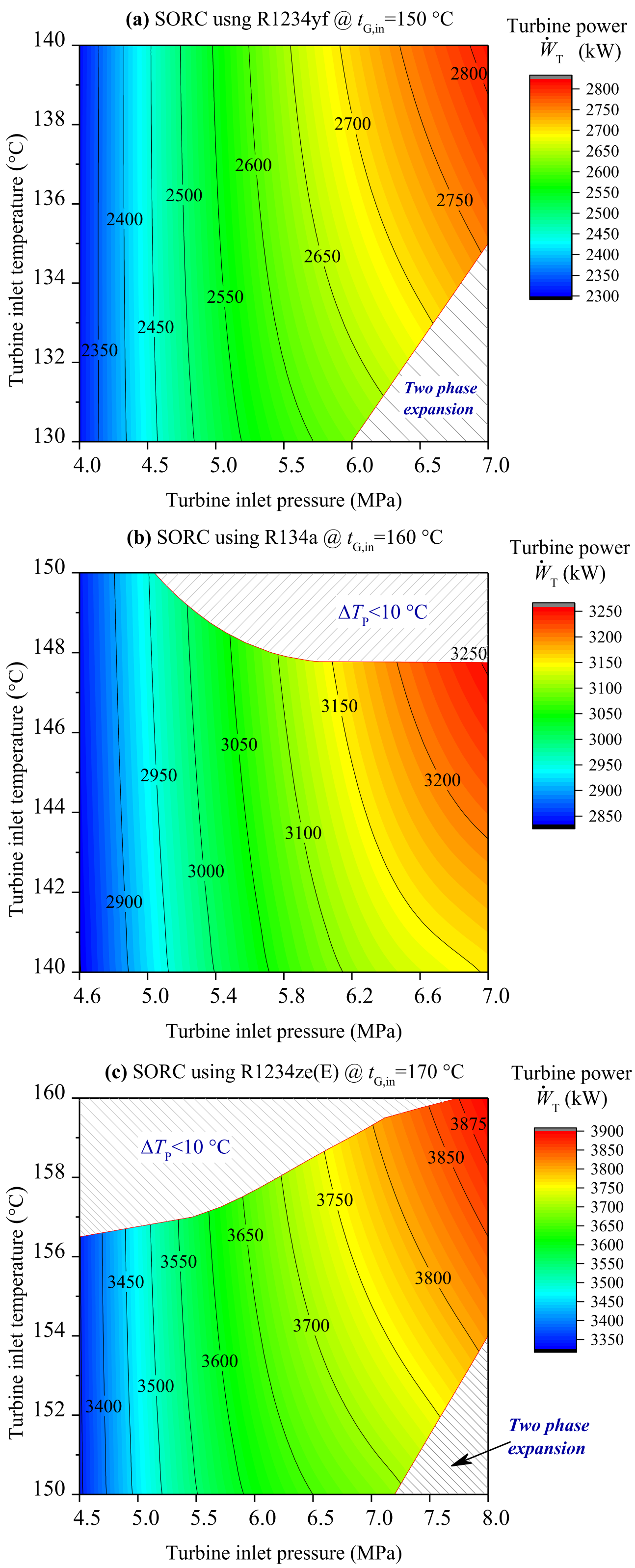

Fig. 6. Turbine power outputs of SORCs with (a) R1234yf, (b) R134a, and (c) R1234ze(E) as functions of turbine inlet temperature and pressure.

Therefore, in SORC systems, both the turbine inlet temperature and pressure should be simultaneously increased to obtain the maximum turbine power output. Specifically, the turbine inlet pressure of R134a is constrained to further increase by the pinch point in the PHE at higher turbine inlet temperatures, as shown in Fig. 6(b). In contrast, the pinch point temperature difference (PPTD) constrains the minimum allowable turbine inlet pressure of R1234ze(E), as illustrated in Fig. 6(c). Notably, for dry and isentropic working fluids, a higher turbine inlet pressure may cause the expansion through vapor-liquid region as shown in Fig. 7(a) and (c), particularly at a lower turbine inlet temperature. Therefore, the turbine inlet parameters should be constrained to avoid two-phase expansion, which can adversely affect turbine performance and reliability. As suggested in Refs. [56,85], a practical approach is to ensure that the turbine inlet entropy remains higher than the turning point of the saturated vapor line defined in Refs. [62,86]. For wet fluids, expansion into the two-phase region typically occurs near the end of the expansion process at higher inlet pressures.

The power consumption by the feed pump significantly increases as the turbine inlet pressure increases due to the increases in mass flow rate and pressure increase. For example, when the inlet pressure is increased from 4 MPa to 7 MPa at an inlet temperature of 136 °C for SORC using R1234yf, the feed pump power consumption increases by 149.4 %, while the turbine power output only increases by 19.8 %. In addition, the power consumption by the cooling system also increases with increasing turbine inlet pressure. Therefore, for a given turbine inlet temperature, there is an optimal inlet pressure that maximizes the net power output, as shown in Fig. 8. As the turbine inlet temperature increases, the corresponding local optimal inlet pressure increases. When the geothermal source temperature is significantly higher than the working fluid (e.g., R1234yf) critical temperature, the optimal turbine inlet temperature tends to approach the upper limit to maximize the net power output, as shown in Fig. 8(a). In the SORC system using R134a driven by geothermal brine at 160 °C, when the turbine inlet temperature exceeds 148 °C, the inlet pressure cannot be excessively high; otherwise, the PPTD between the brine and working fluid falls below the allowable limit. For SORC using R134a, the optimal parameters for maximizing net power output are located along the upper boundary of the contour plot in Fig. 8(b). Conversely, when the turbine inlet temperature exceeds 156.5 °C, the inlet pressure of R1234ze(E) should not be too low; otherwise, the temperature difference between the geothermal brine and the working fluid falls below the specified pinch point threshold due to the increased average heat capacity of the working fluid. As shown by the upper boundary of the contour plot in Fig. 8(c), the corresponding minimum allowable inlet pressure increases with increasing turbine inlet temperature. A global maximum net power output is obtained at the optimal combination of inlet temperature and pressure, which occurs at 157.5 °C and 5.88 MPa for SORC using R1234ze(E) at geothermal brine temperature of 170 °C. Beyond this point, although the turbine power output continues to increase with increasing inlet temperature and pressure, the associated increase in working fluid mass flow rate and pressure leads to a substantial increase in feed pump power consumption and a decrease in net power output.

3.2. Effect of turbine inlet parameters on power output in RSORC

Fig. 9 presents the variation of turbine power output in the RSORC as a function of turbine inlet temperature and pressure. The temperature increase in the recuperator increases the working fluid mass flow rate. To maintain within an acceptable temperature difference between the brine and working fluid, the minimum allowable turbine inlet pressure in the RSORC must be higher than that in the SORC at the same turbine inlet temperature, thereby reducing the average specific heat. Data points at higher turbine inlet pressures are excluded from Fig. 9 due to the excessively low turbine exhaust temperatures, which severely constrain the effectiveness of recuperative heat transfer. The specific enthalpy drop in the turbine generally decreases as the inlet pressure increases at a given inlet temperature and condensing pressure; however, the working fluid mass flow rate remains nearly unchanged, since the reduced average specific heat offsets the increased temperature increase in the PHE. Consequently, unlike in the SORC, the turbine power output in the RSORC tends to decrease with increasing turbine inlet

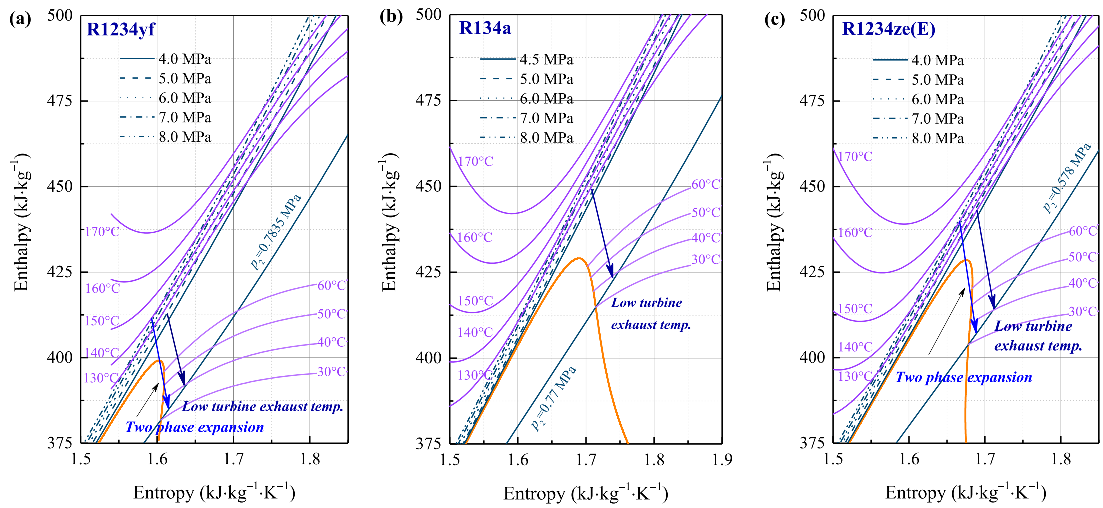

Fig. 7. Enthalpy-entropy diagrams of (a) R1234yf, (b) R134a and (c) R1234ze(E).

pressure at a constant inlet temperature. Notably, the turbine power output initially increases slightly and then decreases with increasing turbine inlet pressure at lower inlet temperatures, as shown in Fig. 9(a) and (b). This non-monotonic behavior is attributed to a similar trend in the specific enthalpy drop. The maximum turbine power output in the RSORC occurs at the highest turbine inlet temperature combined with the corresponding minimum allowable inlet pressure.

Fig. 10 presents the net power outputs of RSORCs as a function of turbine inlet temperature and pressure. For a given turbine inlet temperature, the local maximum net power output occurs at the lowest allowable inlet pressure constrained by the pinch point. This is primarily due to the combined effects of increased pump power consumption and reduced turbine power output as the turbine inlet pressure increases. The influence of turbine inlet pressure on net power output is more pronounced in the RSORC. For instance, in the RSORC using R1234yf at a turbine inlet temperature of 132 °C, the turbine power output is reduced by 0.8 % (23 kW) but the net power output is reduced by 3.2 % (61 kW) as the inlet pressure increases to 5 MPa from 4.7 MPa. Although the turbine power output in the RSORC continues to increase with increasing inlet temperature, the corresponding allowable inlet pressure constrained by the PPTD also increases. This results in higher pump power consumption, leading to an optimal turbine inlet temperature that yields the global maximum net power output. Notably, the net power output presents only slight variation in the vicinity of this optimal temperature. For example, as the turbine inlet temperature increases from 129 °C to 136 °C in RSORC using R1234yf, the net power output increases from 1881 kW to 1894 kW then decreases to 1877 kW at the corresponding minimal inlet pressure, showing a change of less than 1 %.

3.3. *Optimal turbine inlet parameters*

The turbine inlet temperature and pressure were optimized to maximize the net power output for both SORC and RSORC systems, with geothermal brine temperatures ranging from 150 °C to 180 °C and a rejection temperature of 70 °C. The optimal turbine inlet temperatures are shown in Fig. 11, while Fig. 12 presents the optimal turbine inlet pressure with the corresponding reduced inlet pressure shown in Fig. 13. In the SORC system, dry working fluids exhibit higher turbine inlet temperature and reduced turbine inlet pressure (p_1/p_{cr}) to achieve the maximal net power output. The optimal turbine inlet pressure of RC318 is the lowest, but the corresponding reduced pressure is only lower than R1234yf and R227ea. R290 presents the highest optimal turbine inlet pressure, followed by R134a. Notably, the optimal turbine inlet pressures of R1243zf and R1234ze(E) are significantly lower than that of R134a, although their corresponding reduced pressures are close. R152a presents the lowest optimal turbine inlet temperature among the candidates and expands into the two-phase region at geothermal brine temperatures below 172 °C. As the brine temperature further increases, the optimal turbine inlet pressure for R152a decreases, as shown in Fig. 12(a), thereby reducing feed pump power consumption; nevertheless, the expansion process remains entirely within vapor phase.

In the RSORC system, the incorporation of a recuperator increases the working fluid temperature at the PHE inlet, shifting the pinch point toward the low-temperature region of the PHE and thereby constraining the maximum achievable turbine inlet temperature (see Fig. 5). Under a fixed condensing pressure, reducing the turbine inlet pressure increases the specific enthalpy drop across the turbine, decreases feed pump power consumption, and increases the turbine exhaust temperature which enhances the effectiveness of recuperative heat transfer. Moreover, the resulting decrease in turbine inlet temperature and pressure increases the fluid heat capacity rate, further shifting the pinch point to an even lower-temperature region and, in turn, influencing the turbine inlet parameters. Consequently, under the combined effects of pinch point constraints, and variations in thermophysical property, the RSORC exhibits lower optimal turbine inlet temperature and pressure compared to the SORC.

As shown in Fig. 11, the optimal turbine inlet temperature of R1234yf in the RSORC is 7.5–7.9 °C lower than that in the SORC, while for RC318 the reduction reaches 7.9–10.6 °C. For R290, R1243zf and R1234ze(E), the decreases in optimal turbine inlet temperature do not exceed 4.5 °C at a geothermal brine temperature of 150 °C, due to the smaller temperature increases in the recuperator; however, as the brine temperature increases to 180 °C, the reductions reach up to 10 °C. R1234ze(E) exhibits the lowest optimal turbine inlet temperature in the RSORC for brine temperatures below 170 °C, while R134a achieves the highest optimal turbine inlet temperature for higher source temperatures.

As shown in Fig. 12, the reduction in optimal turbine inlet pressure for wet and isentropic working fluids in the RSORC compared to the SORC generally increases as the brine temperature increases. The optimal turbine inlet pressure of R290 in RSORC decreases by 0.35 MPa for a brine temperature of 150 °C, whereas the reduction reaches 0.73 MPa for a brine temperature of 180 °C. In contrast, for dry working fluids, the decrease in optimal turbine inlet pressure in the RSORC decreases with increasing geothermal brine temperature, constrained by the PPTD and further influenced by the larger temperature increase achieved in the recuperator. Specifically, at a brine temperature of 150 °C, the optimal turbine inlet pressure of RC318 is 0.46 MPa lower in the RSORC than in the SORC; however, the reduction decreases to 0.1 MPa at a brine temperature of 180 °C.

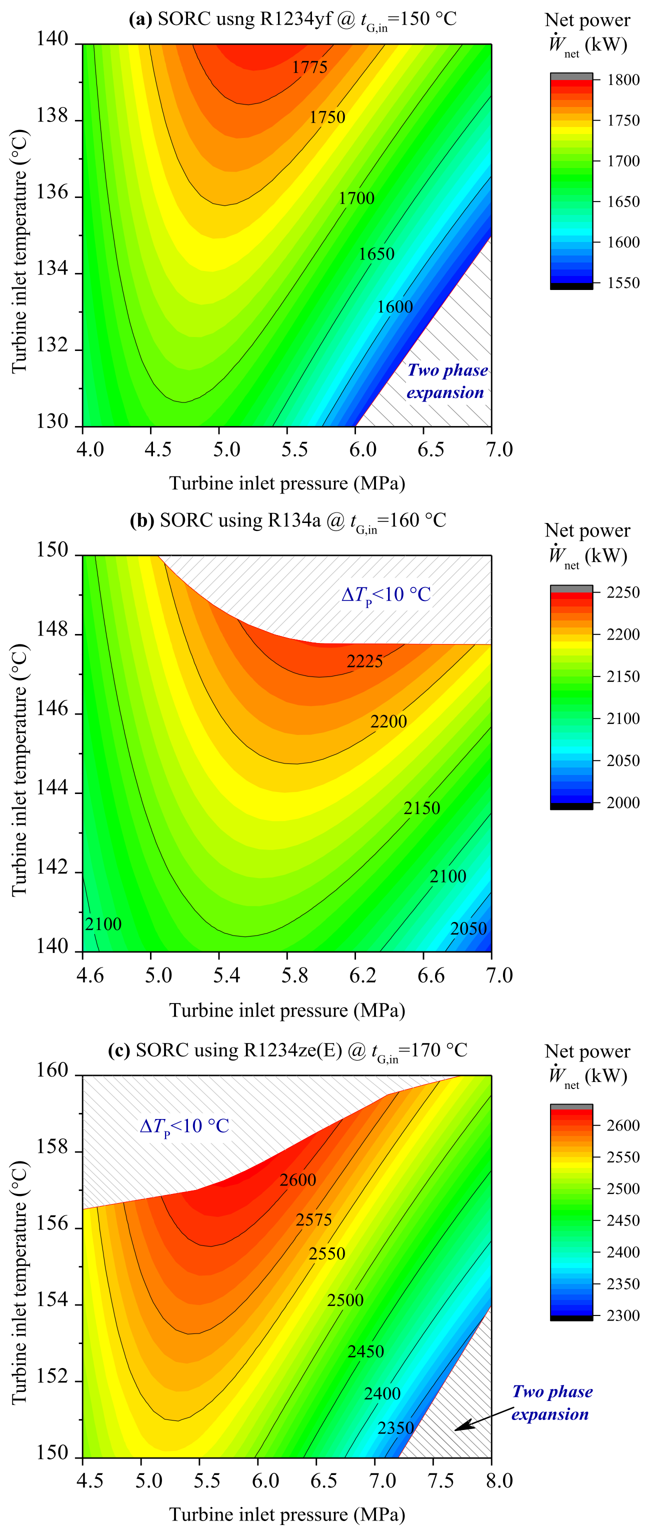

Fig. 8. Net power outputs of SORCs with (a) R1234yf at $t_{G,in}$ = 150 °C, (b) R134a at $t_{G,in}$ = 160 °C, and (c) R1234ze(E) at $t_{G,in}$ = 170 °C as functions of turbine inlet temperature and pressure.

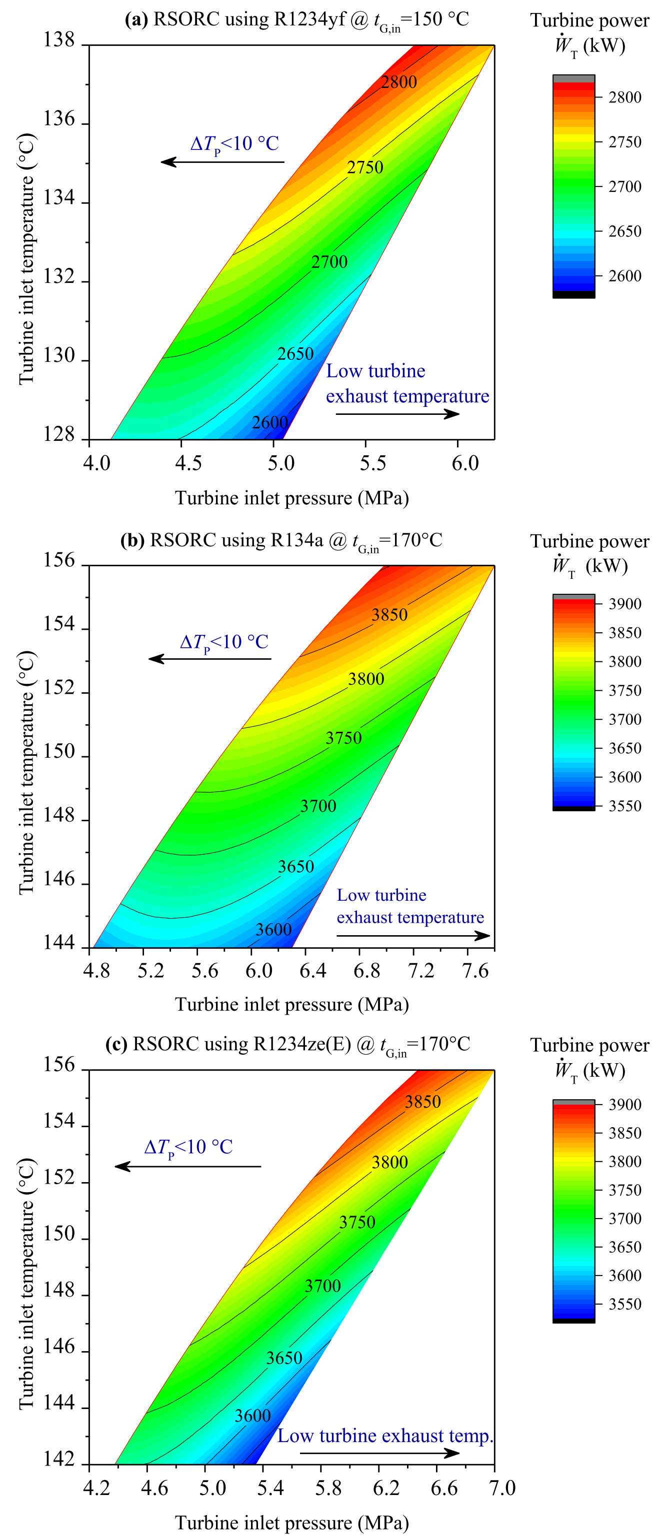

Fig. 9. Turbine power outputs of RSORCs with (a) R1234yf, (b) R134a, and (c) R1234ze(E) as functions of turbine inlet temperature and pressure.

4. Thermodynamic analysis

This section presents a comparative analysis of the net power output, parasitic power consumption (including working fluid pump, circulating pump and cooling tower fan), thermal efficiency, and exergy efficiency of the candidate working fluids under the conditions corresponding to maximum net power output at various geothermal source temperatures. The results are also compared with those of a subcritical ORC with a recuperator using R601a (isopentane) as the working fluid. For the subcritical ORC with saturated vapor at the turbine inlet (hereafter, referred to as SAORC), the evaporation temperatures are optimized to maximize the net power output.

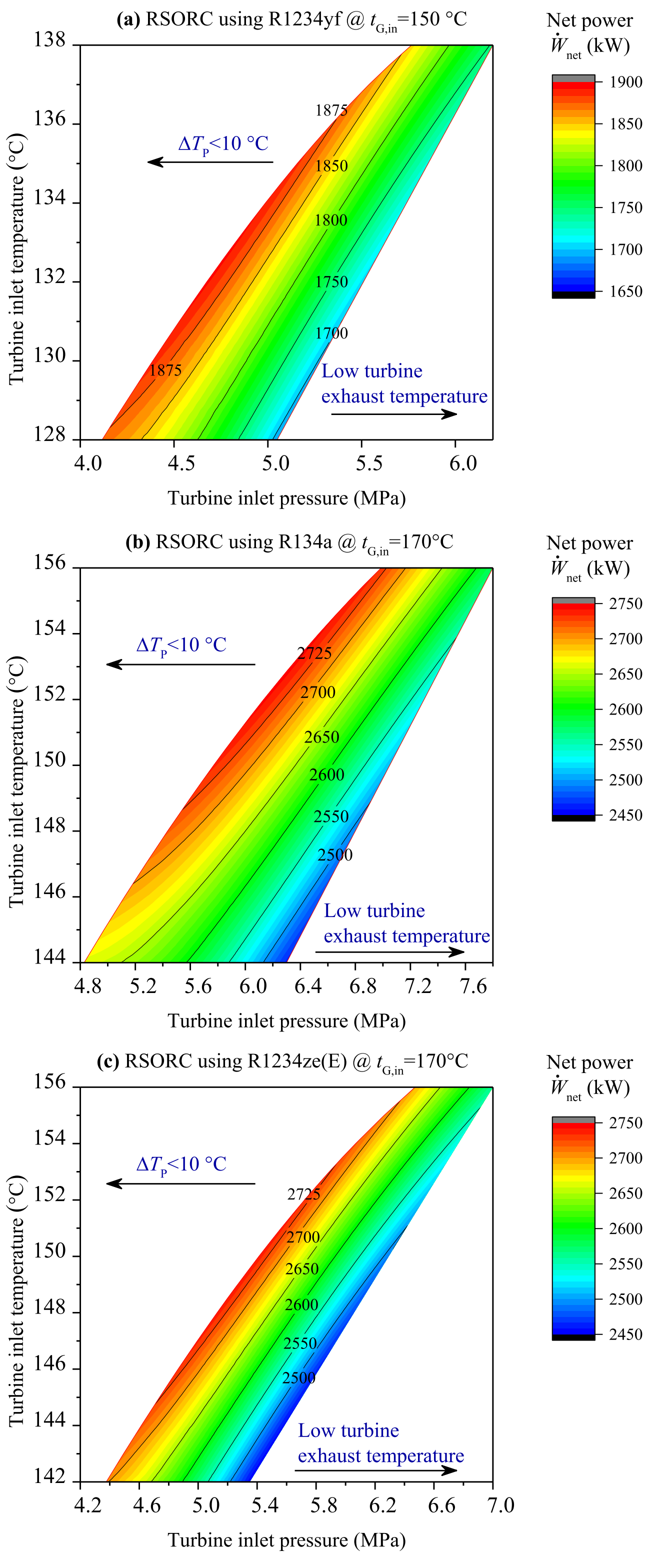

Fig. 10. Net power outputs of RSORCs with (a) R1234yf, (b) R134a, and (c) R1234ze(E) as functions of turbine inlet temperature and pressure.

4.1. Power output

Fig. 14 shows the turbine power outputs of SORCs and RSORCs for the optimal conditions. In the SORC, the specific enthalpy drop of R290 is more than twice that of R134a, R1234yf, R1234ze(E) and R227ea. Consequently, R290 achieves the highest turbine power output despite having the lowest mass flow rate, followed by R134a, as shown in Fig. 14 (a). The turbine power outputs of R1234yf, R1234ze(E) and R152a are comparable to that of R134a at lower brine temperatures, with only a 1–2 % decrease at higher brine temperatures. Although RC318 has the highest mass flow rate among the working fluids, it produces the lowest turbine power due to its lowest enthalpy drop. Additionally, the SORC using R134a achieves 32–37 % higher turbine power output than the SAORC with R601a.

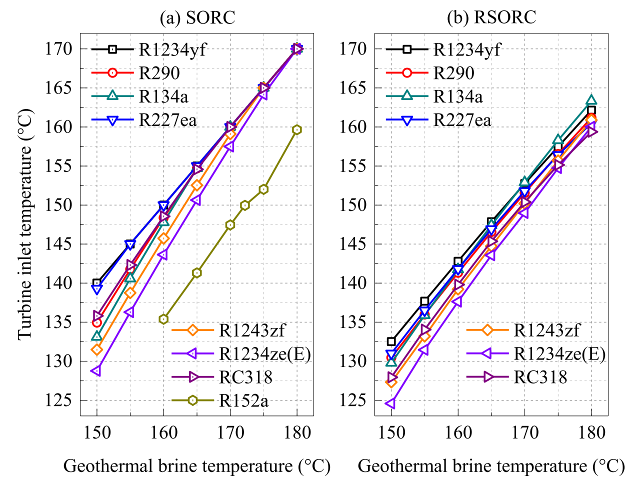

Fig. 11. Optimized turbine inlet temperature for (a) supercritical ORC (SORC) and (b) recuperative SORC (RSORC) for various geothermal brine temperatures.

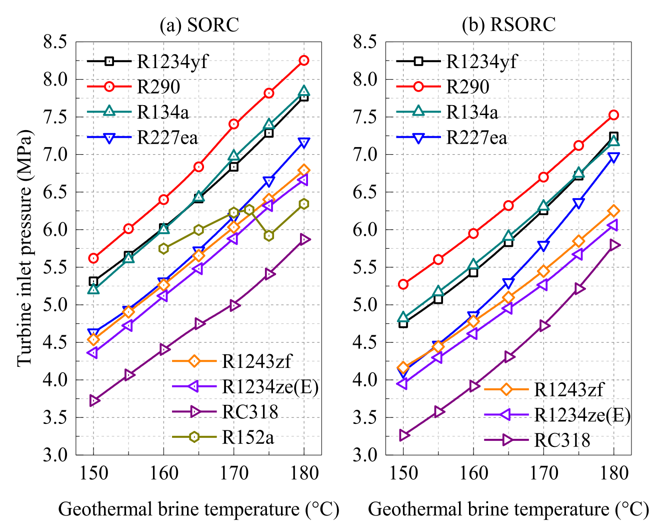

Fig. 12. Optimized turbine inlet pressure of the working fluids for (a) SORC and (b) RSORC for various geothermal brine temperatures.

In the RSORC, both the optimal turbine inlet temperature and pressure are lower than those in the SORC for a given brine temperature, leading to a reduced specific enthalpy drop in the turbine. For instance, the decrease in specific enthalpy drop of RC318 in the RSORC relative to SORC increases from 5.9 % to 9.4 % as the geothermal brine temperature increases from 150 °C to 180 °C. Nevertheless, the turbine power output of RSORC using RC318 increases by 9.9 %–21.7 % compared to SORC, owing to a proportionally larger increase in mass flow rate. Similarly, RSORC using R1234yf produces 5.2–12.5 % more turbine power than SORC. In contrast, for R134a, R1243zf and R1234ze(E), the turbine power outputs in RSORC are almost the same as that in SORC at lower brine temperatures, due to the limited increase in mass flow rate.

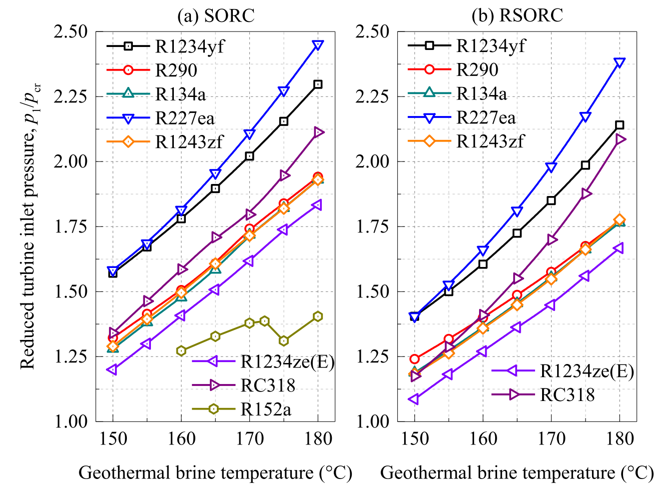

Fig. 13. Reduced turbine inlet pressure for (a) SORC and (b) RSORC at the optimal conditions for various geothermal brine temperatures.

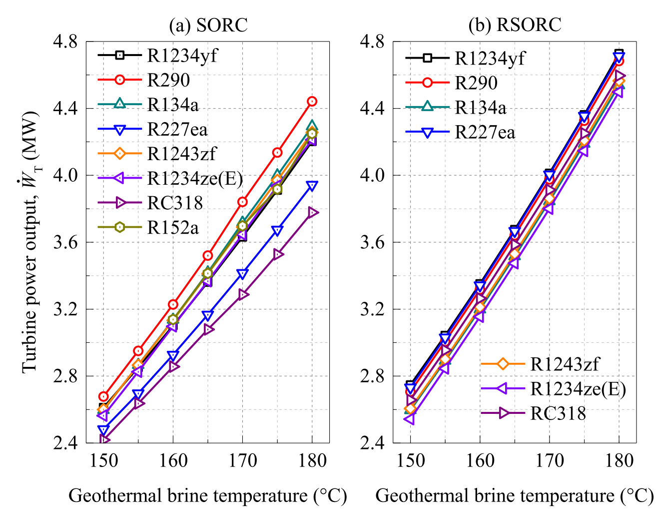

Fig. 14. Turbine power outputs for (a) SORC and (b) RSORC at the optimal conditions for various geothermal water inlet temperatures.

Even at a brine temperature of 180 °C, the turbine power improvements in RSORC for these wet and isentropic working fluids remain modest, at only 5.7–7.3 %. RSORC with R1234yf exhibits the highest turbine power output, slightly outperforming those with R227ea and R290, as shown in Fig. 14(b). Notably, the turbine power output for RSORC using R1234yf is 5.1–8.1 % higher than that using R1234ze(E), with the performance advantage being more pronounced at lower brine temperatures.

Fig. 15 shows the parasitic power fraction relative to the gross turbine power in SORC and RSORC systems. In the SORC using R290, the feed pump exhibits the highest power consumption, accounting for 18.1–21.1 % of the gross turbine power, due to its higher pressure increase and lower density. Feed pump power consumption generally increases with increasing brine temperature. For example, in the SORC using R1234ze(E), the feed pump power fraction increases from 14.1 % to 15.9 %, while in the SORC using R1234yf, it increases from 17.7 % to 21 % as the brine temperature increases from 150 °C to 180 °C. Notably, the SORC with RC318 achieves the lowest feed pump power consumption for brine temperatures below 170 °C, attributed to its lower pressure increase and higher density. However, the feed pump power comsumption for R152a becomes the lowest (only 13.7 % of the gross power) at a brine temperature of 180 °C, due to a reduction in pressure increase. Conversely, the cooling system parasitic load in the SORC with R152a is the highest, driven by increased cooling water and air requirements. In general, SORCs using dry working fluids present lower parasitic power losses from the cooling system compared to those using wet or isentropic working fluids. For example, the cooling system in the SORC with R1234yf consumes 8.4–11.1 % less power than that with R134a. Overall, the cooling system parasitic power accounts for 9.7–11.5 % of gross power at a brine temperature of 150 °C, and 7.4–9.4 % at a brine temperature of 180 °C.

Compared to the SORC, feed pump power consumption in the RSORC decreases at lower brine temperatures due to reduced pressure increase, but increases at higher brine temperatures because of the significant increase in mass flow rate. For instance, the RSORC with R1234ze(E) consumes 10.1 % less pump power than the SROC at a brine temperature of 150 °C, but 4.1 % more at a brine temperature of 180 °C. For dry working fluids, the pressure increase reduction becomes marginal as the brine temperature increases, while the mass flow rate increases substantially, leading to feed pump power consumption increases of up to 26.8 %. In RSORCs using dry working fluids, cooling system power consumption can increase by up to 30 % compared to the SORC, primarily due to increased cooling water demand. The cooling system parasitic load accounts for 10.5–11.6 % of gross power at a brine temperature of 150 °C and 8.1–8.7 % at higher source temperatures. Overall, the total parasitic power requirement amounts to approximately 25 % of the gross turbine power in supercritical ORCs using R134a, compared to only 13.7–16.1 % in the SAORC with R601a.

Fig. 16 shows the maximum net power outputs for SORC and RSORCs for various brine temperatures. In the SORC, R134a produces the highest net power for brine temperatures below 170 °C due to lower parasitic power consumption. The net power outputs of R1243zf and R1234ze(E) are slightly lower, differing by less than 1.2 % from that of R134a. At brine temperatures exceeding 175 °C, SORC using R152a achieves the highest net power output, attributed to its minimal parasitic power demand, which accounts for only 23 % of the turbine power output. Although R290 yields the highest turbine power output among the candidate fluids, 29 % of the turbine power is consumed by the pumps and cooling tower fan, resulting in a net power output 1–1.8 % lower than that of R134a. Wet and isentropic working fluids generally achieve more net power output compared to dry working fluids. As the brine temperature increases, the performance advantage becomes more pronounced. For instance, R134a produces 5.1 % more net power than RC318 at a brine temperature of 150 °C and this advantage expands to 12.2 % at a brine temperature of 170 °C. Notably, R152a produces 14.9 % more net power than RC318 at a brine temperature of 180 °C. Compared to the SAORC using R601a, SORCs using wet or isentropic working fluids present a 11.5–20.3 % increase in net power output, while the SORC with RC318 demonstrates only a marginal 1 % improvement at a brine temperature of 180 °C. These results indicate that wet and isentropic working fluids are more suitable for SORC systems, particularly at higher geothermal source temperatures.

In the RSORC systems, the net power outputs of dry working fluids are significantly increased compared to SORCs. The excess of net power generated by RSORC over SORC increases with increasing brine temperature. For RC318, the net power gain in RSORC compared to SORC increases from 10.7 % at a brine temperature of 150 °C to 17.8 % at a brine temperature of 180 °C. In contrast, RSORCs using wet or isentropic fluids show only modest improvements in net power output due to the lower temperature increase in recuperator and decreases in turbine inlet temperature and pressure. The net power increase in RSORC using R134a or R1234ze(E) is less than 1 % at a brine temperature of 150 °C while reaches 6.3 % at a brine temperature of 180 °C. Additionally, RSORCs achieves 17.5−26.7 % more net power output than the SAORC using R601a. Among all the candidates, RC318 enables RSORC to achieve the highest net power output at brine temperatures below 170 °C, exceeding that of R134a by 1.5–4.4 %. However, R1234ze(E) and R1243zf produce approximately 1 % more net power than RC318 at a brine temperature of 180 °C. Therefore, isentropic working fluids with

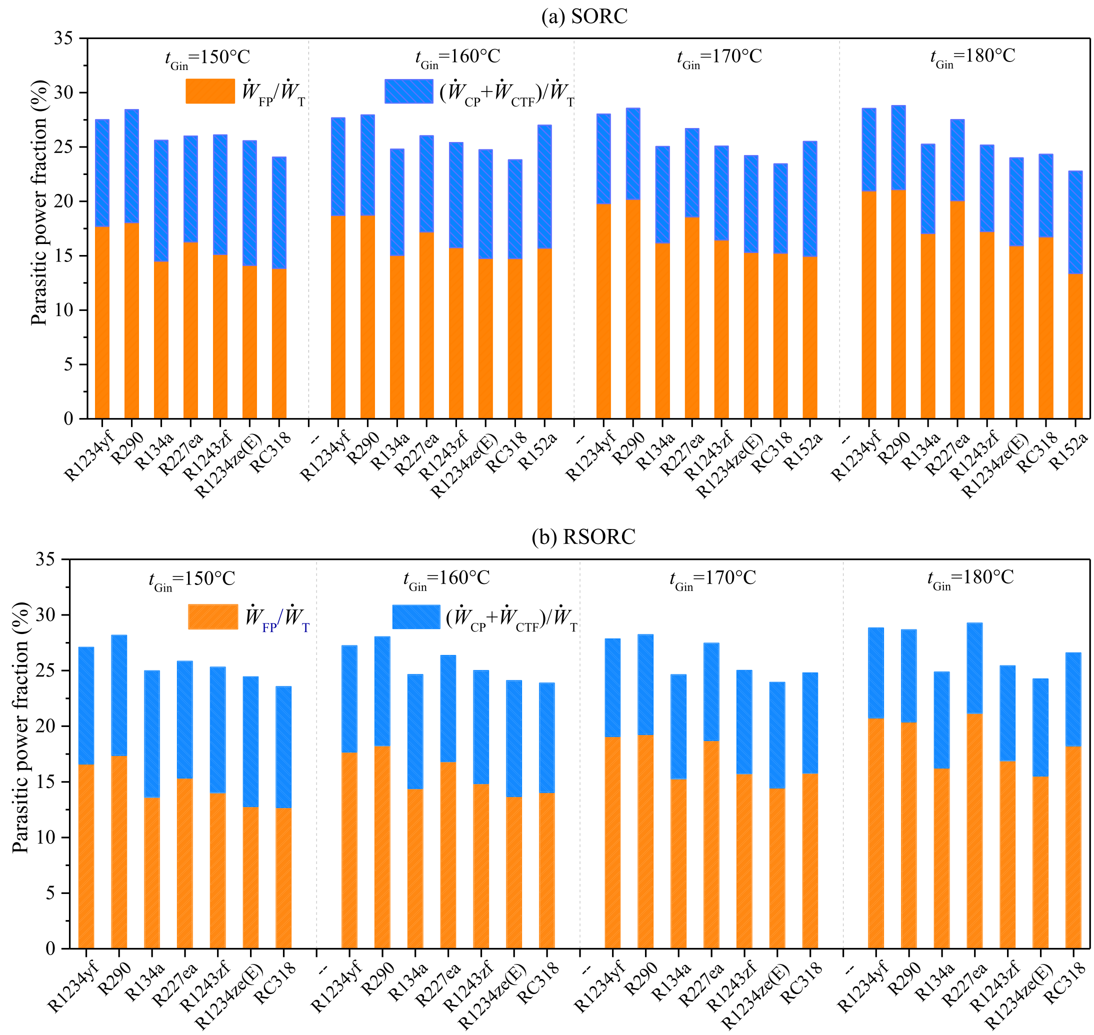

Fig. 15. Parasitic power fraction relative to gross turbine power for (a) SORC and (b) RSORC under optimal conditions.

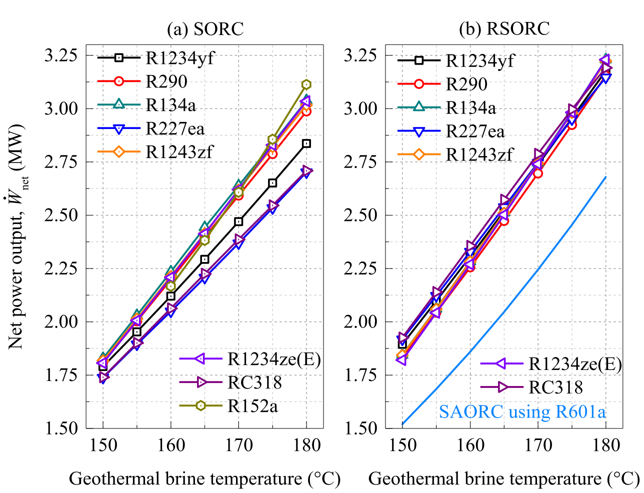

Fig. 16. Net power outputs for (a) SORC and (b) RSORC under optimal conditions at various geothermal brine temperatures.

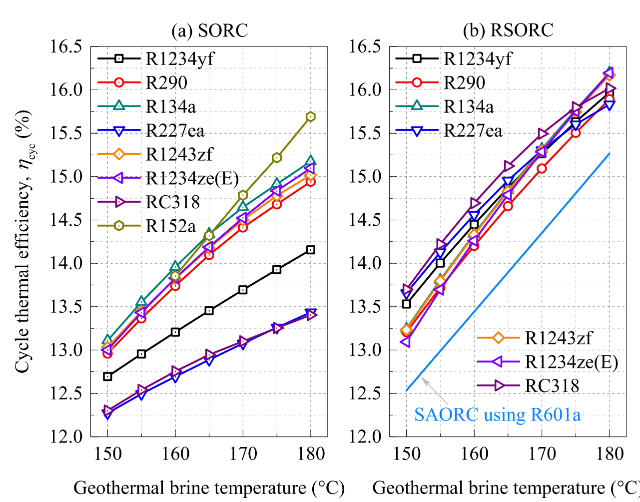

Fig. 17. Cycle thermal efficiencies of (a) SORC and (b) RSORC at the optimal conditions for various geothermal brine temperatures.

higher critical temperatures are preferable for RSORC applications utilizing high-temperature geothermal sources.

4.2. Thermal efficiency

Fig. 17 shows the cycle thermal efficiencies of SORC and RSORC under optimal conditions for various geothermal brine temperatures. In SORC, dry working fluids present lower cycle efficiencies than wet and isentropic working fluids due to greater cold source losses. R134a achieves the highest cycle thermal efficiency for brine temperatures below 165 °C, with a relative improvement of 6.6 %–13.2 % over RC318. For brine temperatures above 165 °C, R152a exhibits superior performance, achieving a 0.9–3.4 % higher cycle efficiency than R134a, attributed to its reduced feed pump power consumption. The SAORC using R601a also achieves higher cycle efficiency than SORCs using dry working fluids, particularly at higher brine temperatures. Notably, the SAORC adopts higher evaporation temperatures to improve cycle efficiency and maximize net power output, but this comes at the cost of reduced geothermal energy utilization efficiency [46,76].

In the RSORC, the incorporation of a recuperator reduces the cold source losses and increases the PHE inlet temperature, thereby significantly improving the cycle efficiency. The efficiency improvement of RSORC relative to SORC increases with increasing brine temperature. For instance, the cycle efficiency of RSORC with R1234yf is 6.6 % higher than that of SORC for a brine temperature of 150 °C and 12.8 % higher for a brine temperature of 180 °C. RC318 achieves the highest cycle efficiency at brine temperatures below 175 °C, while R134a outperforms RC318 by 1.1 % at a brine temperature of 180 °C. Notably, the use of a recuperator improves the cycle thermodynamic completeness, narrowing the cycle efficiency differences among working fluids in the RSORC. Additionally, RSORCs demonstrates a 3.7−9.3 % improvement in cycle efficiency compared to SAORCs using R601a.

Fig. 18 shows the net thermal efficiencies for SORC and RSORC under optimal conditions. The SORC using R134a achieves the highest net thermal efficiency at brine temperatures below 170 °C, while R152a outperforms R134a at brine temperatures above 170 °C. The net thermal efficiencies of R1243zf and R1234ze(E) are very close to that of R134a, with relative differences of less than 1.2 %. In contrast, the relative increase in net thermal efficiency of SORC with R134a over that with R1234yf increases from 2.2 % to 7.1 % as the brine temperature increases from 150 °C to 180 °C. Due to its reduced geothermal heat input, the SAORC using R601a also presents a higher net thermal efficiency than the SORC using RC318.

In the RSORC, dry working fluids generally outperform isentropic and wet working fluids in terms of net thermal efficiencies at lower geothermal brine temperatures. The net thermal efficiency of RSORC with RC318 is 5.8 % higher than that with R1234ze(E) at a brine temperature of 150 °C. However, the efficiency advantage of dry working fluids diminishes at higher brine temperatures. The net thermal efficiency of RSORC with RC318 is 1.2 % lower than that with R1234ze(E), while RSORC with R227ea presents the lowest efficiency at a brine temperature of 180 °C. Notably, the net thermal efficiencies of RSORC using R1234ze(E), R1243zf and R134a converge and show minimal variation at higher brine temperatures. RSORCs present 3.9–11.2 % higher net thermal efficiency than SAORCs with R601a, as shown in Fig. 18(b).

4.3. Exergy analysis

Fig. 19 shows the exergy efficiencies of SORC and RSORC under optimal conditions, with the corresponding exergy destruction rates in components shown in Fig. 20. Exergy losses are primarily distributed among the brine reinjection, primary heat exchanger (PHE), condenser (including the cooling system), and turbine-generator unit. The irreversibility associated with the brine reinjection remains constant across cycles due to the fixed reinjection temperature for a given heat source. SORCs using dry working fluids exhibit lower net exergy efficiencies due to higher exergy losses in the condenser, whereas wet and isentropic working fluids perform better. For example, the condenser exergy destruction rate for RC318 increases from 19.1 % to 22.8 % as the brine temperature increases from 150 °C to 180 °C; however, for R134a, it increases slightly from 16.9 % to 17.3 %. Exergy losses in the PHE account for 11.4–15.3 % of the geothermal exergy input. Wet and isentropic working fluids present lower irreversibility losses in the PHE compared to RC318 and R227ea, particularly at higher brine temperatures. For instance, the exergy destruction rate in the PHE for SORC with R134a decreases from 14.3 % to 12.3 % as the brine temperature increases from 150 °C to 180 °C, while for SORC with RC318, it decreases from 15.3 % to 13.9 %. However, dry working fluids show lower exergy losses in the turbine-generator unit. In SORC with RC318, turbine-generator exergy losses account for 9.8 % of the geothermal exergy input, whereas for R152a, the exergy destruction rate ranges from 11.5 % to 12.6 %. Overall, R134a exhibits the highest exergy efficiency at brine temperatures below 170 °C, while R152a achieves the highest efficiency above 170 °C. Due to the higher irreversibility losses during evaporation and brine reinjection, the exergy efficiencies of SAORCs using R601a are 11.8–16.8 % lower than those of SORCs using R134a.

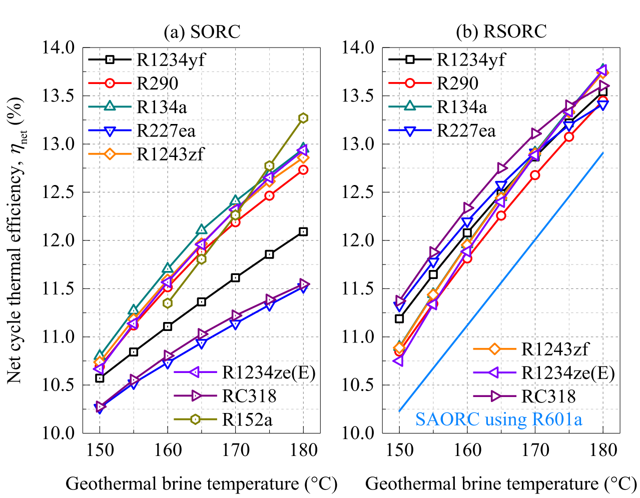

Fig. 18. Net thermal efficiencies of (a) SORC and (b) RSORC at optimal conditions for various geothermal brine temperatures.

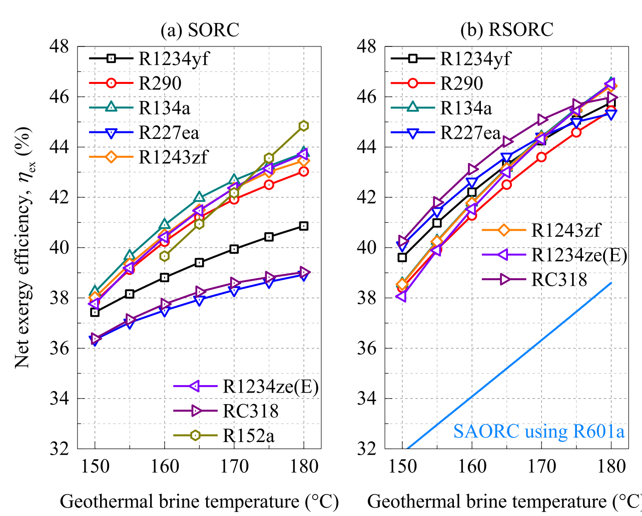

Fig. 19. Exergy efficiencies of SORC and RSORC at the optimal conditions for various geothermal brine temperatures.

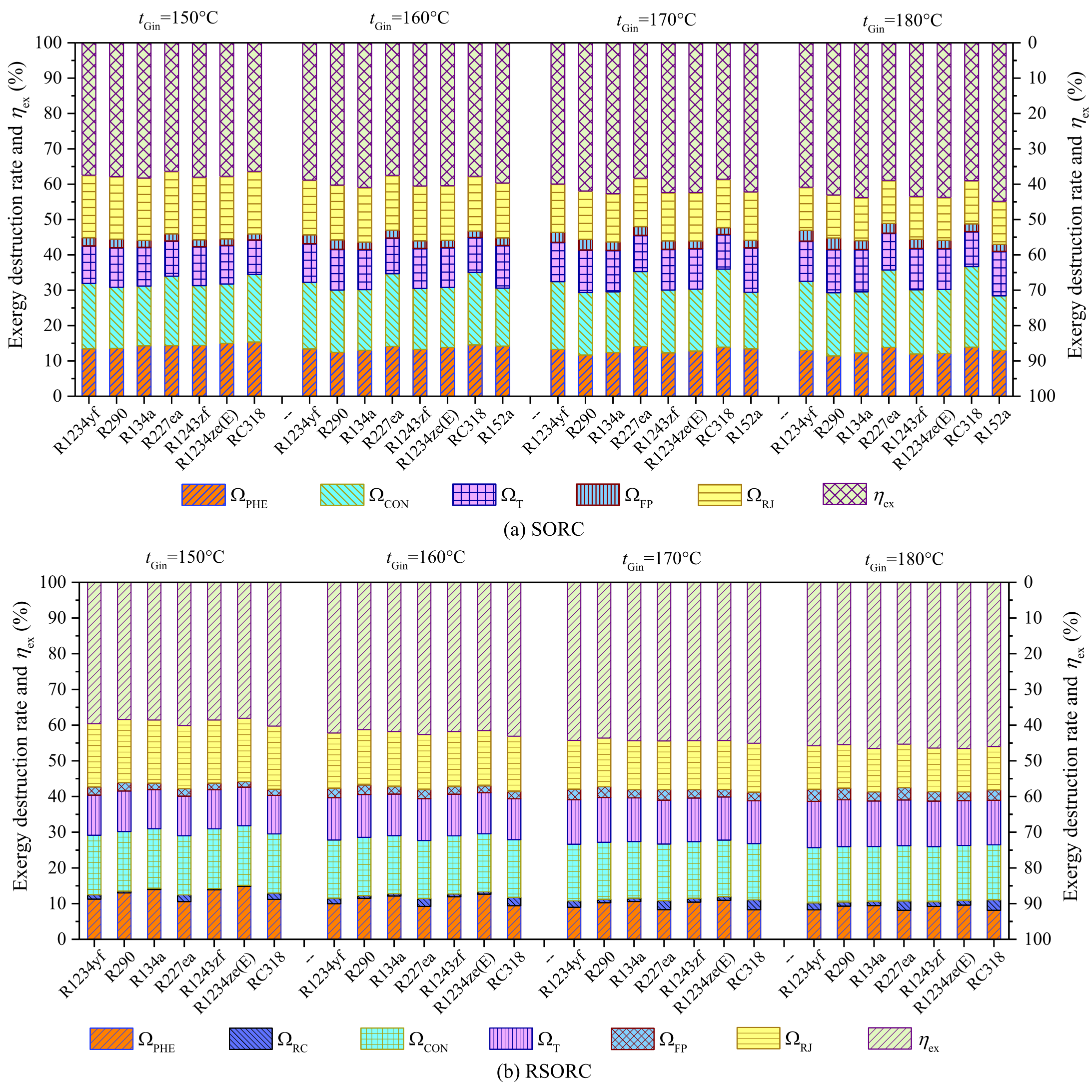

Fig. 20. Exergy destruction rates for the components in (a) SORC and (b) RSORC for the optimal conditions.

Significant reductions in irreversibility losses in the PHE are observed in RSORCs using dry working fluids. Compared to the SORC, the exergy losses in the PHE for RSORC with RC318 decrease by 27 % at a brine temperature of 150 °C and by 41.4 % at a brine temperature of 180 °C. In contrast, the corresponding reductions for RSORC with wet or isentropic working fluids do not exceed 23 %. Additionally, the condenser exergy destruction rate in RSORC with RC318 is 13.5 % lower than that in the SORC at a brine temperature of 150 °C and 32.3 % lower at a brine temperature of 180 °C, whereas the reductions for wet or isentropic fluids only range from 0.4 % to 15 %. Therefore, RSORCs using RC318 exhibit the highest exergy efficiency at brine temperatures below 170 °C, followed by R227ea and R1234yf. However, the total exergy losses in the recuperator and PHE for the RSORC with RC318 exceed those of the RSORC with R1234ze(E) for a brine temperature of 180 °C, leading to a 1.2 % reduction in exergy efficiency.

5. Economic analysis

5.1. Heat exchanger area

Fig. 21 shows the required heat exchanger areas for SORC and RSORC systems. R152a presents the highest heat transfer coefficient (HTC) among the candidates in the PHE due to its turbine inlet pressure being closer to the critical pressure, amplifying the specific heat peak, along with its high thermal conductivity and low viscosity. R134a ranks second in HTC, requiring 11–17 % more PHE area than R152a. R1234ze (E) achieves 1–4.3 % smaller PHE area than R134a for brine temperatures below 170 °C owing to higher LMTD, but 4.7–7.1 % larger area due to its lower HTC and reduced LMTD for brine temperatures above 170 °C. In contrast, dry working fluids exhibit weaker specific heat enhancement due to their higher reduced pressures, resulting in lower HTCs than the selected wet and isentropic working fluids. R1234yf requires 17.4 % greater PHE area than R134a for a brine temperature of 150 °C owing to the lowest LMTD, but 1.2–3.1 % less area at brine temperatures above 165 °C as LMTD improves.

R152a, R134a, and R290 possess higher latent heat, saturated liquid densities, and thermal conductivities, combined with lower viscosities, which collectively enhance condensate film mobility and heat conduction, resulting in superior condensation performance. R152a achieves the highest condensation HTC, followed by R134a and R290. However, R152a requires 6.8–11.4 % larger condenser area than R134a, because of its greater condensation heat load. Conversely, dry working fluids achieve comparable or even reduced condenser areas (up to 4.4 % smaller than R134a), due to their lower condensing heat loads, despite inferior condensation HTCs. For a geothermal brine inlet temperature of 150 °C, the condenser areas for R1234ze(E) are about 6 % larger than that for R134a, while at a brine temperature of 180 °C, the required condenser areas are nearly identical. Among the candidate fluids, R290

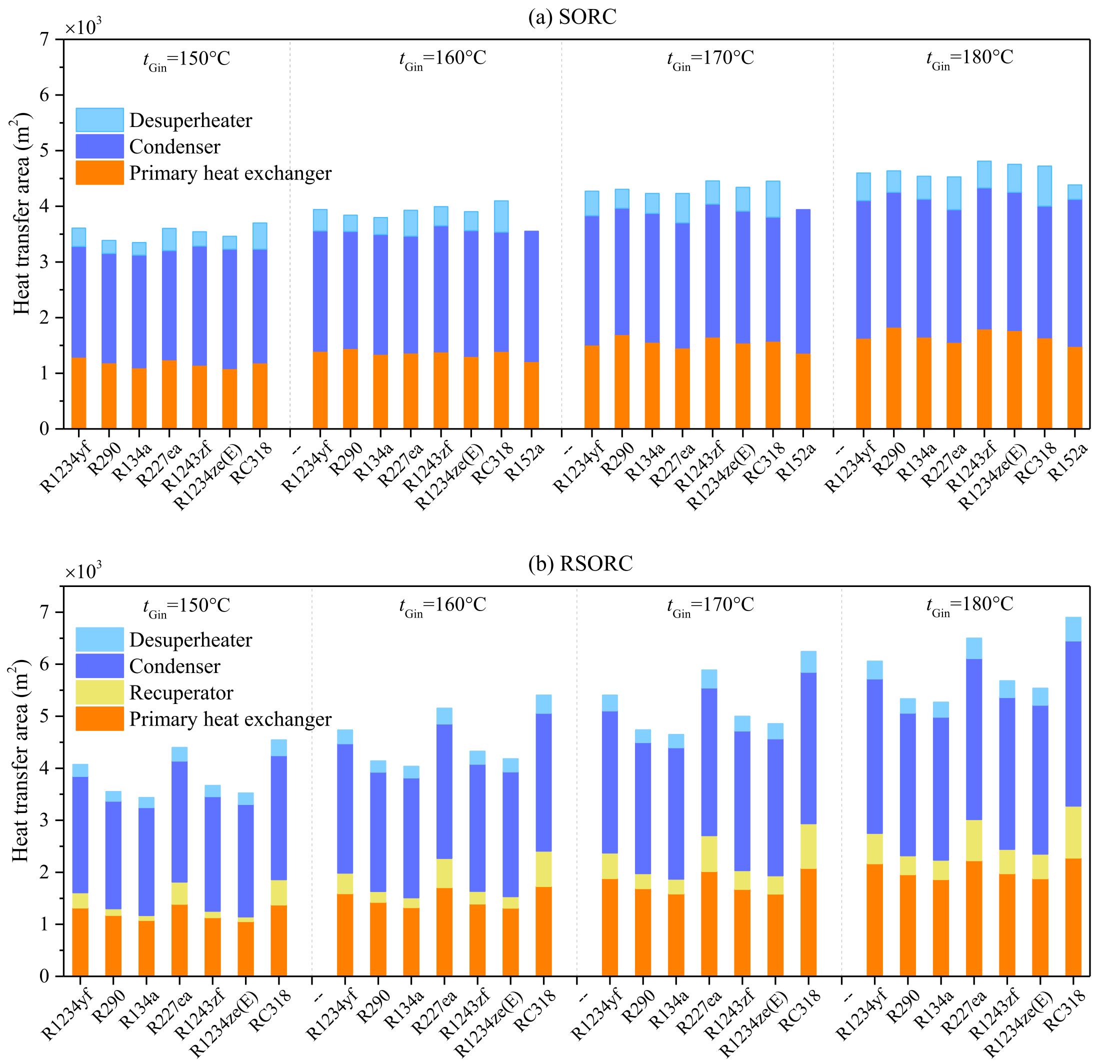

Fig. 21. Required heat transfer areas for (a) SORC and (b) RSORC at the optimal condition.

achieves the highest HTC in the desuperheater due to its higher specific heat capacity and thermal conductivity, requiring 3.5–6.4 % less desuperheater area than R134a for brine temperatures above 160 °C, despite a 14–20 % higher heat load. Dry and isentropic fluids require larger desuperheater areas than wet fluids because of their inherently higher heat loads. RC318 presents the lowest HTC, attributed to its low specific heat and thermal conductivity, combined with the highest heat load, demands the largest desuperheater area. For R1234yf, although its heat load is 1.5–2.2 times greater than that of R134a, its higher HTC and LMTD limit the desuperheater area increase to 19.7–46.2 %.

In the SORC system, dry working fluids require up to 10.5 % more total heat exchanger area than R134a at a brine temperature of 150 °C, with the gap narrowing to 1–4 % at 180 °C. R1234ze(E) requires 2.1–4.7 % more total area compared to R134a. In contrast, R152a demands the lowest total heat exchanger area, 3.4–7.2 % lower than that of R134a. For the SAORC, R601a requires 9 % more total area than R134a at a brine temperature of 180 °C due to a larger desuperheater, but 2–4 % less at lower brine temperatures.

Compared with SORC, the optimal turbine inlet pressure in RSORC is lower, leading to a reduced pseudo-critical temperature and a more pronounced peak in specific heat, which enhances the HTC near the pseudo-critical point. However, in the PHE high-temperature section, the HTC decreases due to reduced density and thermal conductivity. Wet and isentropic working fluids require smaller PHE areas in RSORC than in SORC for brine temperatures below 160 °C, because of the larger temperature difference in the high-temperature section. In contrast, dry working fluids consistently demand larger PHE areas in RSORC due to the lower overall HTC. R1234yf requires 1.9 % more PHE area in RSORC at a brine temperature of 150 °C, while it requires 32.6 % additional area at 180 °C. In RSORC, the PHE area for R1234ze(E) is close to that for R134a, while R1234yf requires 16.3 %–22 % more area.

The RSORC system requires a larger condenser area than the SORC system due to the increased condensation heat load. For R134a, the condenser area in RSORC is 2.4–11.2 % greater than that in SORC. As the geothermal brine temperature increases from 150 °C to 180 °C, the additional condenser area required for RSORC using R1234yf relative to SORC increases from 12.5 % to 20.2 %. This growth is even more pronounced for RC318, with RSORC requiring 34.3 % more condenser area at a brine temperature of 180 °C. In RSORC, the condenser area required for R1234ze(E) is approximately 4 % larger than that for R134a. Compared to the SORC system, the desuperheater area in RSORC is reduced up to 38 %. However, the additional recuperator area contributes to an increase in the total heat exchanger area, particularly for dry working fluids. At a brine temperature of 150 °C, the recuperator area required for R1234yf is approximately 3 times that of R134a, while for RC318, it can be up to 5 times larger. As the geothermal brine temperature increases to 180 °C, R1234yf requires 57 % more, and RC318 requires 169 % more recuperator area compared to R134a.

In RSORC, R134a requires 2.7−16.1 % more total heat exchanger area than that in SORC, due to the increased condenser and additional recuperator areas; nevertheless, it remains the smallest among the evaluated working fluids. RC318 demands the largest total heat exchanger area in RSORC, exceeding that in SORC by 22.8–46.1 %. The total area required for R290 is comparable to that of R134a, while R1234ze(E) requires 2.5–5.1 % more. In contrast, dry working fluids require 15–34 % more total area than R134a.

5.2. Specific investment cost

Fig. 22 shows the bare module costs which include both direct and indirect costs of the major components and Fig. 23 illustrates the specific investment costs (SICs) for the SORC and RSORC systems. SORC using R134a presents the lowest SIC at brine temperatures below 165 °C, while that using R152a achieves the lowest SIC at higher geothermal source temperatures, primarily due to its lower heat exchanger and working fluid feed pump costs. The heat exchanger costs for dry working fluids are higher than those of R134a, particularly at lower brine temperatures, but the cooling system costs are up to 8.8 % lower.

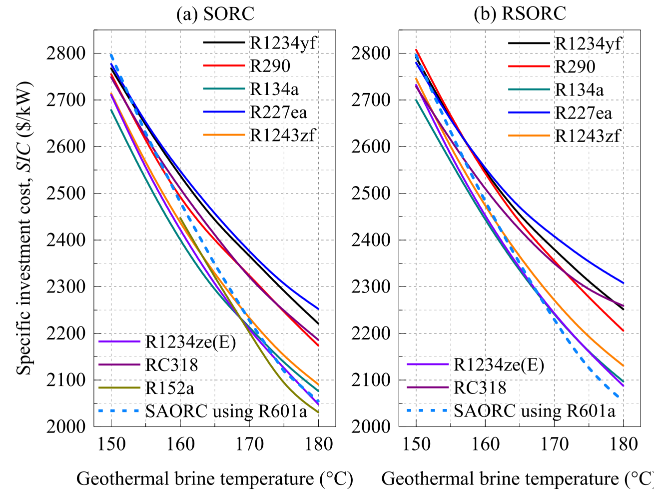

Fig. 23. Specific investment costs of (a) SORC and (b) RSORC.

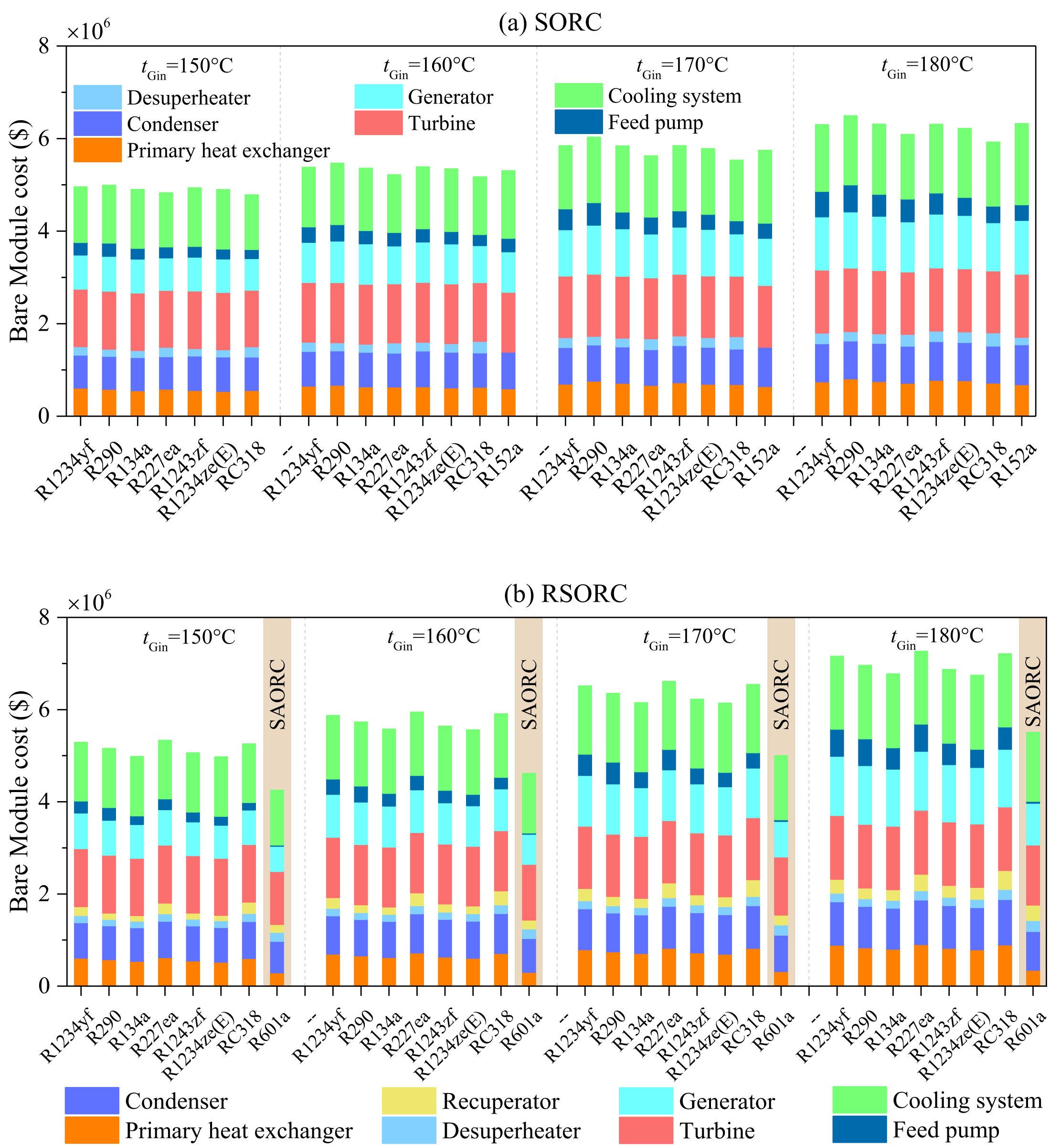

Fig. 22. Bare module costs of components for (a) SORC and (b) RSORC.

Consequently, the total equipment investments for SORC with dry working fluids are comparable to those of R134a; however, their SICs remain 2.6−8.5 % higher. Notably, the SORC using R1234ze(E) achieves an SIC 1.4 % lower than R134a at higher brine temperatures, owing to reduced pump and cooling system costs, but this advantage diminishes when accounting for the relatively high cost of R1234ze(E). The SICs of SORC systems are lower than that of the SAORC using R601a at a brine temperature of 150 °C, but only SORC with R152a and R1234ze(E) maintain lower SICs for higher source temperatures.

In the RSORC system using a wet or isentropic fluid, the PHE cost is lower than that in the SORC at brine temperatures below 170 °C due to the reduced operating pressure. By contrast, RSORCs with dry working fluids present higher PHE cost compared to SORCs; for instance, the PHE cost for RC318 increases by up to 26.4 %. The total heat exchanger cost in RSORCs increases significantly with increasing brine temperatures. For example, the heat exchanger cost in the RSORC using R134a increases by 7.8 % at a brine temperature of 150 °C and 17.4 % at a brine temperature of 180 °C, while the corresponding increase for R1234yf ranges from 14.8 % to 28.9 %. The turbine cost in RSORC increases by less than 3 %, but the generator cost increases by up to 20 %. Cooling system costs also increase, particularly for RSORCs with dry working fluids (5.8–14.9 %), compared with only 1.2–7.9 % for wet and isentropic fluids. In contrast, RSORCs require lower feed pump costs than SORCs, with reductions of up to 19 % at lower source temperatures. Overall, the total equipment costs of RSORCs using dry working fluids are 6.7–21.8 % higher than those of SORCs, while RSORCs with wet or isentropic fluids present moderate cost increases of 1.6–8.9 %. Nevertheless, because of the higher net power output, the SIC of RSORCs increases slightly compared to SORC, with the maximum increase limited to 3.3 %. Specifically, the SICs for RSORC with R134a or R1234ze(E) remain lower than that of the SAORC using R601a at brine temperatures below 165 °C, but become 2 % higher at a brine temperature of 180 °C.

6. Conclusions

The turbine inlet temperature and pressure of selected working fluids were optimized to maximize the net power outputs for supercritical ORCs (SORCs) and recuperative SORCs (RSORCs), driven by geothermal brine temperatures ranging from 150 °C to 180 °C with a reinjection temperature of 70 °C. The thermodynamic and economic performance of the SORC and RSORC using various working fluids was analyzed. The results show that:

SORC systems output the maximum turbine power at the highest achievable inlet temperature and pressure. Wet working fluids outperform dry fluids owing to lower cold source losses. Among the candidates, R290 yields the highest turbine power; however, its parasitic power consumption accounts for 29 % of the gross power, reducing the net power output. For brine temperatures below 170 °C, R134a achieves the highest net power output and the lowest specific investment cost (SIC). For higher brine temperatures, R152a exhibits superior performance due to its minimal parasitic power demand. R1234ze(E) and R1243zf emerge as promising alternatives, offering net power outputs and SICs comparable to those of R134a with benefits of lower optimal turbine inlet pressure and reduced environmental impacts.

In RSORC systems, enhanced recuperative heat transfer improves the thermodynamic completeness and shifts the pinch point toward the low-temperature region in the PHE, thereby limiting the achievable turbine inlet temperature and pressure. The maximum turbine power is obtained at the highest feasible turbine inlet temperature and the lowest allowable pressure constrained by the PPTD. Although the total parasitic power fraction relative to gross power slightly decreases in RSORC, the cooling system still consumes more power than in the SORC. Dry working fluids yield 5.8–17.8 % more net power than in SORC, while wet or isentropic fluids offer a modest increase of 1–6.8 %. Despite an up to 21 % increase in total investment cost, the SIC of RSORC increases only slightly due to the increased net power output. At brine temperatures below 170 °C, RC318 achieves the highest net power, while R1234ze(E) outperforms RC318 at higher temperatures with a 1 % gain in net power. Moreover, the improved thermal matching in the RSORC reduces the net power differences among working fluids. R1234ze(E) achieves up to 9 % lower SIC than the selected dry working fluids, emerging as the most promising working fluid for RSORC.

CRediT authorship contribution statement

Qiang Liu: Writing – review & editing, Writing – original draft, Visualization, Validation, Resources, Project administration, Methodology, Investigation, Funding acquisition, Formal analysis. **Fufang Yang:** Writing – review & editing, Writing – original draft, Visualization, Investigation, Formal analysis. **Xiong Liu:** Writing – review & editing, Resources, Funding acquisition. **Xiaodong Zhang:** Writing – original draft, Resources. **Zuowei Yang:** Writing – review & editing, Formal analysis.

Financial support

This research was funded by the National Major Science and Technology Project of China (Grant No. 2024ZD1003506) and the National Natural Science Foundation of China (Grant No. 51506223).

Declaration of competing interest

The authors declare that they have no known competing financial interests or personal relationships that could have appeared to influence the work reported in this paper.

References

[1] L.C.A. Gutiérrez-Negrín, Evolution of worldwide geothermal power 2020–2023, Geotherm. Energy 12 (2024) 14, https://doi.org/10.1186/s40517-024-00290-w.

[2] J. Jello, T. Baser, Utilization of existing hydrocarbon wells for geothermal system development: a review, Appl. Energy 348 (2023) 121456, https://doi.org/10.1016/j.apenergy.2023.121456.

[3] R. DiPippo, Geothermal Power Plants: Principles, Applications, Case Studies and Environmental Impact, third ed., Elsevier, 2012.

[4] C. Spadacini, L.G. Xodo, M. Quaia, 14 - geothermal energy exploitation with Organic Rankine Cycle technologies, in: E. Macchi, M. Astolfi (Eds.), Organic Rankine Cycle (ORC) Power Systems, Woodhead Publishing, 2017, pp. 473–525, https://doi.org/10.1016/B978-0-08-100510-1.00014-4.

[5] G. Mines, 13 - binary geothermal energy conversion systems: basic Rankine, dual−pressure, and dual-fluid cycles, in: R. DiPippo (Ed.), Geothermal Power Generation, Woodhead Publishing, 2016, pp. 353–389, https://doi.org/10.1016/B978-0-08-100337-4.00013-9.

[6] A. Basaran, L. Ozgerer, Investigation of the effect of different refrigerants on performances of binary geothermal power plants, Energy Convers. Manag. 76 (2013) 484–498, https://doi.org/10.1016/j.enconman.2013.07.058.

[7] T.L. Li, Z.G. Zhang, J. Lu, J.L. Yang, Y.J. Hu, Two-stage evaporation strategy to improve system performance for organic Rankine cycle, Appl. Energy 150 (2015) 323–334, https://doi.org/10.1016/j.apenergy.2015.04.016.

[8] K. Braimakis, S. Karellas, Exergetic optimization of double stage Organic Rankine Cycle (ORC), Energy 149 (2018) 296–313, https://doi.org/10.1016/j.energy.2018.02.044.

[9] Y. Du, Y. Yang, D. Hu, M. Hao, J.F. Wang, Y.P. Dai, Off-design performance comparative analysis between basic and parallel dual-pressure organic Rankine cycles using radial inflow turbines, Appl. Therm. Eng. 138 (2018) 18–34, https://doi.org/10.1016/j.applthermaleng.2018.04.036.

[10] X.L. Yang, Z.C. Yan, S.J. Bu, W.K. Li, C. Su, X. Wang, et al., Performance analysis, multiobjective optimization and working fluid selection for a DPORC system with geothermal source shunting, Therm. Sci. Eng. Prog. 47 (2024) 102267, https://doi.org/10.1016/j.tsep.2023.102267.

[11] Z. Guzović, P. Rašković, Z. Blatarić, The comparision of a basic and a dual-pressure ORC (Organic Rankine Cycle): geothermal Power Plant Velika Ciglena case study, Energy 76 (2014) 175–186, https://doi.org/10.1016/j.energy.2014.06.005.

[12] S.K. Wang, C. Liu, C. Zhang, X.X. Xu, Q.B. Li, Thermo-economic evaluations of dual pressure organic Rankine cycle (DPORC) driven by geothermal heat source, J. Renew. Sustain. Energy 10 (2018) 063901, https://doi.org/10.1063/1.5034062.

[13] G. Manente, A. Lazzaretto, E. Bonamico, Design guidelines for the choice between single and dual pressure layouts in organic Rankine cycle (ORC) systems, Energy 123 (2017) 413–431, https://doi.org/10.1016/j.energy.2017.01.151.

[14] N. Chagnon-Lessard, F. Mathieu-Potvin, L. Gosselin, Optimal design of geothermal power plants: a comparison of single-pressure and dual-pressure organic Rankine

cycles, Geothermics 86 (2020) 101787, https://doi.org/10.1016/j.geothermics.2019.101787.
[15] G. Angelino, P. Colonna di Paliano, Multicomponent working fluids for organic Rankine cycles (ORCs), Energy 23 (1998) 449–463, https://doi.org/10.1016/S0360-5442(98)00009-7.
[16] M.J. Bai, L. Zhao, R.K. Zhao, Review on applications of zeotropic mixtures, J. Therm. Sci. 31 (2) (2022) 285–307, https://doi.org/10.1007/s11630-022-1569-x.
[17] Q. Liu, A.J. Shen, Y.Y. Duan, Parametric optimization and performance analyses of geothermal organic Rankine cycles using R600a/R601a mixtures as working fluids, Appl. Energy 148 (2015) 410–420, https://doi.org/10.1016/j.apenergy.2013.11.036.
[18] F. Heberle, M. Preibinger, D. Brüggemann, Zeotropic mixtures as working fluids in organic Rankine cycles for low-enthalpy geothermal resources, Renew. Energy 37 (2012) 364–370, https://doi.org/10.1016/j.renene.2011.06.044.
[19] Q. Liu, Y. Duan, Z. Yang, Effect of condensation temperature glide on the performance of organic Rankine cycles with zeotropic mixture working fluids, Appl. Energy 115 (2014) 394–404.
[20] K. Braimakis, V. Grispos, S. Karellas, Exergetic efficiency potential of double-stage ORCs with zeotropic mixtures of natural hydrocarbons and CO2, Energy 218 (2021) 119577, https://doi.org/10.1016/j.energy.2020.119577.
[21] Y. Chen, Y.X. Liu, E. Nam, Y. Zhang, A. Dahlak, Exergoeconomic and exergoenvironmental analysis and optimization of an integrated double-flash-binary geothermal system and dual-pressure ORC using zeotropic mixtures; multi-objective optimization, Energy 283 (2023) 128367, https://doi.org/10.1016/j.energy.2023.128367.
[22] A.H. Mosaffa, A new combined power and dual ejector refrigeration system using zeotropic mixtures with composition adjustable driven by geothermal resource: an exergoeconomic performance evaluation, Geothermics 108 (2023) 102629, https://doi.org/10.1016/j.geothermics.2022.102629.
[23] X.L. Luo, R.L. Huang, Z. Yang, J.Y. Chen, Y. Chen, Performance investigation of a novel zeotropic organic Rankine cycle coupling liquid separation condensation and multi-pressure evaporation, Energy Convers. Manag. 161 (2018) 112–127, https://doi.org/10.1016/j.enconman.2018.01.070.
[24] P. Lu, X.L. Luo, J. Wang, J.Y. Chen, Y.Z. Liang, Z. Yang, et al., Thermo-economic design, optimization, and evaluation of a novel zeotropic ORC with mixture composition adjustment during operation, Energy Convers. Manag. 230 (2021) 113771, https://doi.org/10.1016/j.enconman.2020.113771.
[25] C.W. Liu, T.Y. Gao, Off-design performance analysis of basic ORC, ORC using zeotropic mixtures and composition-adjustable ORC under optimal control strategy, Energy 171 (2019) 95–108, https://doi.org/10.1016/j.energy.2018.12.195.
[26] I. Smith, Development of the trilateral flash cycle system. part 1: fundamental considerations, Proc. Inst. Mech. Eng. Part A J Power Energy 207 (3) (1993) 179–194, https://doi.org/10.1243/PIME_PROC_1993_207_032_02.
[27] C. Zamfirescu, I. Dincer, Thermodynamic analysis of a novel-ammonia-water trilateral Rankine cycle, Thermochim. Acta 477 (2008) 7–15, https://doi.org/10.1016/j.tca.2008.08.002.
[28] R. DiPippo, Ideal thermal efficiency for geothermal binary plants, Geothermics 36 (3) (2007) 276–285, https://doi.org/10.1016/j.geothermics.2007.03.002.
[29] J. Fischer, Comparison of trilateral cycles and organic Rankine cycles, Energy 36 (10) (2011) 6208–6219, https://doi.org/10.1016/j.energy.2011.07.041.
[30] S. Lecompte, H. Huisseune, M. van den Broek, M. De Paepe, Methodical thermodynamic analysis and regression models of organic Rankine cycle architectures for waste heat recovery, Energy 87 (2015) 60–76, https://doi.org/10.1016/j.energy.2015.04.094.
[31] S. Daniarta, P. Kolasiński, A.R. Imre, Thermodynamic efficiency of trilateral flash cycle, organic Rankine cycle and partially evaporated organic Rankine cycle, Energy Convers. Manag. 249 (2021) 114731, https://doi.org/10.1016/j.enconman.2021.114731.
[32] Z.L. Wang, H. Shao, M.C. Shao, Z.Y. Dai, R. Zhang, Thermodynamic analysis of a coupled system based on total flow cycle and partially evaporated organic Rankine cycle for hot dry rock utilization, Renew. Energy 225 (2024) 120272, https://doi.org/10.1016/j.renene.2024.120272.
[33] F. Dawo, J. Buhr, C. Schifflechner, C. Wieland, H. Spliethoff, Experimental assessment of an organic Rankine cycle with a partially evaporated working fluid, Appl. Therm. Eng. 221 (2023) 119858, https://doi.org/10.1016/j.applthermaleng.2022.119858.
[34] Y. Zhou, F. Zhang, L. Yu, Performance analysis of the partial evaporating organic Rankine cycle (PEORC) using zeotropic mixtures, Energy Convers. Manag. 129 (2016) 89–99, https://doi.org/10.1016/j.enconman.2016.10.009.
[35] K. Braimakis, S. Karellas, Exergy efficiency potential of dual-phase expansion trilateral and partial evaporation ORC with zeotropic mixtures, Energy 262 (2023) 125475, https://doi.org/10.1016/j.energy.2022.125475.
[36] A. Skiadopoulos, G. Kosmadakis, S. Lecompte, M.D. Paepe, D. Manolakos, Numerical modeling of flashing in TFC expanders for the efficient exploitation of low-grade heat, Therm. Sci. Eng. Prog. 46 (2023) 102171, https://doi.org/10.1016/j.tsep.2023.102171.
[37] T. Ho, S.S. Mao, R. Greif, Increased power production through enhancements to the organic flash cycle (OFC), Energy 45 (1) (2012) 686–695, https://doi.org/10.1016/j.energy.2012.07.023.
[38] C. Wu, X.X. Xu, Q.B. Li, X.X. Li, L. Liu, C. Liu, Performance assessment and optimization of a novel geothermal combined cooling and power system integrating an organic flash cycle with an ammonia-water absorption refrigeration cycle, Energy Convers. Manag. 227 (2021) 113562, https://doi.org/10.1016/j.enconman.2020.113562.
[39] D.Y. Meng, Q. Liu, Z.L. Ji, Performance analyses of regenerative organic flash cycles for geothermal power generation, Energy Convers. Manag. 224 (2020) 113396, https://doi.org/10.1016/j.enconman.2020.113396.
[40] A.H. Mosaffa, A. Zareei, Proposal and thermoeconomic analysis of geothermal flash binary power plants utilizing different types of organic flash cycle, Geothermics 72 (2018) 47–63, https://doi.org/10.1016/j.geothermics.2017.10.011.
[41] A. Baccioli, M. Antonelli, U. Desideri, Technical and economic analysis of organic flash regenerative cycles (OFRCs) for low temperature waste heat recovery, Appl. Energy 199 (2017) 69–87, https://doi.org/10.1016/j.apenergy.2017.04.058.
[42] D.Y. Meng, Q. Liu, Z.L. Ji, Effects of two-phase expander on the thermoeconomics of organic double-flash cycles for geothermal power generation, Energy 239 (2022) 122346, https://doi.org/10.1016/j.energy.2021.122346.
[43] N. Meng, T.L. Li, X. Gao, Q.H. Liu, X.L. Li, H.Y. Gao, Thermodynamic and techno-economic performance comparison of two-stage series organic Rankine cycle and organic Rankine flash cycle for geothermal power generation from hot dry rock, Appl. Therm. Eng. 200 (2022) 117715, https://doi.org/10.1016/j.applthermaleng.2021.117715.
[44] T.L. Li, Y. Zhang, X.L. Li, Y. Yuan, Techno-economic comparison of organic fluid between single- and dual-flash for geothermal power generation enhancement, Renew. Energy 231 (2024) 120917, https://doi.org/10.1016/j.renene.2024.120917.
[45] A. Schuster, S. Karellas, R. Aumann, Efficiency optimization potential in supercritical organic Rankine cycles, Energy 35 (2) (2010) 1033–1039, https://doi.org/10.1016/j.energy.2009.06.019.
[46] C. Augustine, R. Field, R. DiPippo, G. Gigliucci, I. Fastelli, J. Tester, Modeling and analysis of sub- and supercritical binary Rankine cycles for low- to mid-temperature geothermal resources, GRC Trans. 33 (2009) 689–693.
[47] R. DiPippo, K. Kitz, Geothermal binary power plants at Raft River, San Emidio, and Neal Hot Springs: part 1 — plant descriptions and design performance comparison, GRC Trans. 39 (2015) 833–846.
[48] Z. Gu, H. Sato, Performance of supercritical cycles for geothermal binary design, Energy Convers. Manag. 43 (7) (2002) 961–971, https://doi.org/10.1016/S0196-8904(01)00082-6.
[49] A. Toffolo, A. Lazzaretto, G. Manente, M. Paci, A multi-criteria approach for the optimal selection of working fluid and design parameters in Organic Rankine Cycle systems, Appl. Energy 121 (2014) 219–232, https://doi.org/10.1016/j.apenergy.2014.01.089.
[50] S. Lecompte, E. Ntavou, B. Tchanche, G. Kosmadakis, A. Pillai, D. Manolakos, M. De Paepe, Review of experimental research on supercritical and transcritical thermodynamic cycles designed for heat recovery application, Appl. Sci. 9 (12) (2019) 2571, https://doi.org/10.3390/app9122571.
[51] C. Invernizzi, P. Bombarda, Thermodynamic performance of selected HCFS for geothermal applications, Energy 22 (9) (1997) 887–895, https://doi.org/10.1016/S0360-5442(97)00004-2.
[52] R. Vidhi, S. Kuravi, Y.D. Goswami, E. Stefanakos, A.S. Sabau, Organic fluids in a supercritical Rankine cycle for low temperature power generation, ASME. J. Energy Res. Technol. 135 (4) (2013) 042002, https://doi.org/10.1115/1.4023513.
[53] F. Moloney, E. Almatrafi, D.Y. Goswami, Working fluid parametric analysis for recuperative supercritical organic Rankine cycles for medium geothermal reservoir temperatures, Renew. Energy (2020) 2874–2881, https://doi.org/10.1016/j.renene.2018.09.003.
[54] M.Z. Lukawski, J.W. Tester, R. DiPippo, Impact of molecular structure of working fluids on performance of organic Rankine cycles (ORCs), Sustain. Energy Fuels 1 (2017) 1098–1111, https://doi.org/10.1039/c6se00064a.
[55] F. Yang, F. Yang, Q. Liu, Q. Chu, Z. Yang, Y. Duan, Thermodynamic analysis of working fluids: what is the highest performance of the sub-and trans-critical organic Rankine cycles? Energy 241 (2022) 122512 https://doi.org/10.1016/j.energy.2021.122512.
[56] X.C. Wang, E.K. Levy, C.J. Pan, C.E. Romero, A. Banerjee, C. Rubio-Maya, L.H. Pan, Working fluid selection for organic Rankine cycle power generation using hot produced supercritical CO2 from a geothermal reservoir, Appl. Therm. Eng. 149 (2019) 1287–1304, https://doi.org/10.1016/j.applthermaleng.2018.12.112.
[57] N. Zhang, Q. Wang, Z. Yu, G. Yu, A non-structural fuzzy decision method developed for organic Rankine cycles used in liquid-dominated geothermal fields of medium/high temperature, Energy Convers. Manag. 231 (2021) 113861, https://doi.org/10.1016/j.enconman.2021.113861.
[58] A.S. Chowdhury, M.M. Ehsan, A critical overview of working fluids in organic Rankine, supercritical Rankine, and supercritical Brayton cycles under various heat grade sources, Int. J. Thermofluids 20 (2023) 100426, https://doi.org/10.1016/j.ijft.2023.100426.
[59] H.J. Chen, D.Y. Goswami, M.M. Rahman, E. Stefanakos, A supercritical Rankine cycle using zeotropic mixture working fluids for the conversion of low-grade heat into power, Energy 36 (1) (2011) 549–555, https://doi.org/10.1016/j.energy.2010.10.006.
[60] H.B. Yin, A.S. Sabau, J.C. Conklin, J. McFarlane, A.L. Qualls, Mixtures of SF6–CO2 as working fluids for geothermal power plants, Appl. Energy 106 (2013) 243–253, https://doi.org/10.1016/j.apenergy.2013.01.060.
[61] J. Radulovic, N.I. Beleno Castaneda, On the potential of zeotropic mixtures in supercritical ORC powered by geothermal energy source, Energy Convers. Manag. 88 (2014) 365–371, https://doi.org/10.1016/j.enconman.2014.08.048.
[62] Q. Liu, R. Chen, X.L. Yang, X. Xiao, Thermodynamic analyses of sub- and supercritical ORCs using R1234yf, R236ea and their mixtures as working fluids for geothermal power generation, Energies 16 (15) (2023) 5676, https://doi.org/10.3390/en16155676.
[63] C. Wu, S.S. Wang, X. Jiang, J. Li, Thermodynamic analysis and performance optimization of transcritical power cycles using CO2-based binary zeotropic

mixtures as working fluids for geothermal power plants, Appl. Therm. Eng. 115 (2017) 292–304, https://doi.org/10.1016/j.applthermaleng.2016.12.077.
[64] G. Manente, L. Da Lio, A. Lazzaretto, Influence of axial turbine efficiency maps on the performance of subcritical and supercritical Organic Rankine Cycle systems, Energy 107 (2016) 761–772, https://doi.org/10.1016/j.energy.2016.04.063.
[65] D. Maraver, J. Royo, V. Lemort, S. Quoilin, Systematic optimization of subcritical and transcritical organic Rankine cycles (ORCs) constrained by technical parameters in multiple applications, Appl. Energy 117 (2014) 11–29, https://doi.org/10.1016/j.apenergy.2013.11.076.
[66] V.L. Le, M. Feidt, A. Kheiri, S. Pelloux-Prayer, Performance optimization of low-temperature power generation by supercritical ORCs (organic Rankine cycles) using low GWP (global warming potential) working fluids, Energy 67 (2014) 513–526, https://doi.org/10.1016/j.energy.2013.12.027.
[67] M. Astolfi, M.C. Romano, P. Bombarda, E. Macchi, Binary ORC (organic Rankine cycles) power plants for the exploitation of medium-low temperature geothermal sources – Part A: thermodynamic optimization, Energy 66 (2014) 423–434, https://doi.org/10.1016/j.energy.2013.11.056.
[68] M. Astolfi, M.C. Romano, P. Bombarda, E. Macchi, Binary ORC (organic Rankine cycles) power plants for the exploitation of medium-low temperature geothermal sources – Part B: Techno-economic optimization, Energy 66 (2014) 435–446, https://doi.org/10.1016/j.energy.2013.11.057.
[69] J. Song, P. Loo, J. Teo, C.N. Markides, Thermo-Economic Optimization of Organic Rankine Cycle (ORC) systems for geothermal power generation: a comparative study of system configurations, Front. Energy Res. 8 (2020) 6, https://doi.org/10.3389/fenrg.2020.00006.
[70] Q.G. Wang, T.Z. Ming, Q. Chen, Y.J. Wu, A novel TLFD-GA algorithm for multi-objectives optimization of ORC power plants with the effect of pressure drop considered, Energy 293 (2024) 130652.
[71] F. Heberle, C. Schifflechner, D. Brüggemann, Life cycle assessment of Organic Rankine Cycles for geothermal power generation considering low-GWP working fluids, Geothermics 64 (2016) 392–400, https://doi.org/10.1016/j.geothermics.2016.06.010.
[72] E.G. Huo, L.Y. Xin, S.K. Wang, Thermal stability and pyrolysis mechanism of working fluids for organic Rankine cycle: a review, Int. J. Energy Res. 46 (2022) 19313–20900, https://doi.org/10.1002/er.8518.
[73] X.Y. Dai, L. Shi, Q.S. An, W.Z. Qian, Thermal stability of some hydrofluorocarbons as supercritical ORCs working fluids, Appl. Therm. Eng. 128 (2018) 1095–1101, https://doi.org/10.1016/j.applthermaleng.2017.09.046.
[74] R. Gunawan, M.Z. Irriyanto, H.S. Cahyadi, M. Irshad, H.S. Lim, B.S. Choi, et al., Mechanism of thermal decomposition of HFO-1234ze(E) under supercritical fluid conditions, J. Supercrit. Fluids 160 (2020) 104792, https://doi.org/10.1016/j.supflu.2020.104792.
[75] C.M. Invernizzi, D. Bonalumi, Thermal stability of organic fluids for Organic Rankine Cycle systems, in: E. Macchi, M. Astolfi (Eds.), Organic Rankine Cycle (ORC) Power Systems, Woodhead Publishing, 2017, pp. 121–151, https://doi.org/10.1016/B978-0-08-100510-1.00005-3.
[76] Q. Liu, Y.Y. Duan, Z. Yang, Performance analyses of geothermal organic Rankine cycles with selected hydrocarbon working fluids, Energy 63 (2013) 123–132.
[77] E.W. Lemmon, I.H. Bell, M.L. Huber, M.O. McLinden, Reference fluid thermodynamic and transport properties (REFPROP), NIST Standard Reference Database 23 (Version 10.0) (2018).
[78] Q. Liu, J. Song, Y.Y. Duan, Comparative thermodynamic analyses of Rankine cycles using different working fluids for LNG cold energy recovery, Case Stud. Therm. Eng. 69 (2025) 105952, https://doi.org/10.1016/j.csite.2025.105952.
[79] S. Mokry, I. Pioro, A. Farah, K. King, S. Gupta, W. Peiman, et al., Development of supercritical water heat-transfer correlation for vertical bare tubes, Nucl. Eng. Des. 241 (4) (2011) 1126–1136, https://doi.org/10.1016/j.nucengdes.2010.06.012.
[80] D. Jung, S. Chae, D. Bae, S. Oho, Condensation heat transfer coefficients of flammable refrigerants, Int. J. Refrig. 27 (2004) 314–317, https://doi.org/10.1016/j.ijrefrig.2003.09.006.
[81] V. Gnielinski, New equations for heat and mass transfer in turbulent pipe and channel flows, Int. Chem. Eng. 16 (1976) 359–368.
[82] S.W. Churchill, M. Bernstein, A correlating equation for forced convection from gases and liquids to a circular cylinder in crossflow, J. Heat Tran. 99 (1977) 300–306, https://doi.org/10.1115/1.3450685.
[83] R. Turton, J.A. Shaeiwitz, D. Bhattacharyya, W.B. Whiting, Analysis, Synthesis and Design of Chemical Processes, fifth ed., Pearson Education, Inc., 2018.
[84] H. Sayyadi, M. Nejatolahi, Thermodynamic and thermoeconomic optimization of a cooling tower-assisted ground source heat pump, Geothermics 40 (3) (2011) 221–232, https://doi.org/10.1016/j.geothermics.2011.06.003.
[85] Y. Ren, L.B. Yang, Y.W. Cao, B. Wang, J.Z. Chen, J.X. Shi, Study on the performance and multi-objective optimization of supercritical Organic Rankine cycle system for geothermal power generation, Energy Convers. Manag. 338 (2025) 119915, https://doi.org/10.1016/j.enconman.2025.119915.
[86] X. Zhang, Y. Zhang, Z. Li, J. Wang, Y. Wu, C. Ma, Zeotropic Mixture selection for an organic Rankine cycle using a single screw expander, Energies 13 (5) (2020) 1022, https://doi.org/10.3390/en13051022.

Nomenclature

A: Heat transfer area (m^2)
C: cost ($)
c_p: Specific heat ($kJ\bullet kg^{-1}\ K^{-1}$)
d: Diameter (m)
$\dot{E}$: Exergy (kW)
H: Pump head (m)
h: Specific enthalpy ($kJ\bullet kg^{-1}$)
$\dot{I}$: Exergy destruction (kW)
$\dot{m}$: Mass flow rate ($kg\bullet s^{-1}$)
p: Pressure (MPa)
$\dot{Q}$: Heat flow (kW)
r: Latent heat ($J\bullet kg^{-1}$)
s: Specific entropy ($kJ\bullet kg^{-1}\ K^{-1}$)
T: Temperature (K)
t: Temperature (°C)
U: Overall heat transfer coefficient ($W\bullet m^{-2}\ K^{-1}$)
$\dot{W}$: Power (kW)

Acronyms

FP: Feed pump
G: Generator
GWP: Global warming potential
HTC: Heat transfer coefficient
Nu: Nusselt number
ORC: Organic Rankine cycle
PHE: Primary heat exchanger
PPTD: Pinch point temperature difference
Pr: Prandtl number
Re: Reynold number
RSORC: Recuperative SORC
SAORC: Saturated organic Rankine cycle
SORC: Supercritical organic Rankine cycle
SIC: Specific investment cost

Greek symbols

α: Heat transfer coefficient ($W\bullet m^{-2}\ K^{-1}$)
η: Efficiency (%)
λ: thermal conductivity ($W\cdot m^{-1}\ K^{-1}$)
ρ: Density ($kg\bullet m^{-3}$)
μ: Dynamic viscosity (Pa·s)
Ω: Exergy destruction rate (%)

Subscripts

0: Reference dead state
a: air
b: bulk
CON: condenser
CP: Circulating water pump
CTF: Cooling tower fan
CW: Cooling water
cyc: cycle
ex: Exergy
FP: Feed pump
G: Geothermal brine
Gin: Geothermal brine inlet
Gout: Geothermal brine outlet
i: State points number
in: inlet
max: maximum
min: minimum
MO: motor
net: net
O: Organic working fluid
out: outlet
RC: recuperator
RJ: reinjection
SL: Saturated liquid
SV: Saturated vapor
T: Turbine
th: thermal
w: wall